

ELECTRONICS RESEARCH AT MSFC

May 26, 1966

By

Dorrance L. Anderson
George A. Bailey
James F. Blanche
James L. Hayes
Robert L. Kurtz
T. C. Lawson
Owen Rowe

TABLE OF CONTENTS

OPTICAL ANGULAR DEVIATIONS OF 6328Å RADIATION CAUSED BY REFRACTIVE AND TURBULENT EFFECTS OF THE ATMOSPHERE

by Robert L. Kurtz and James L. Hayes

	Page
SUMMARY	1
LIST OF SYMBOLS	1
INTRODUCTION	1
DESCRIPTION OF SIGNAL DETECTION SYSTEM AND METHOD OF SIGNAL PROCESSING	2
Transfer Curve	2
System Operation	2
Signal Processing	3
PRESENTATION OF DATA	3
Procedure	3
Data Analysis	3
CONCLUSIONS	7
REFERENCES	7

LIST OF TABLES

Table	Title	Page
I.	RMS Values for 0 to 15 Hz for Case I	3
II.	RMS Values for 0 to 15 Hz for Case II	5

LIST OF ILLUSTRATIONS

Figure	Title	Page
1.	Transfer Curve	2
2.	Block Diagram of Signal Detection System	2
3.	Fitted Normal Distributions - Case I	4
4.	Composite Amplitude Density - Case I	5
5.	Fitted Normal Distributions - Case II	6
6.	Composite Amplitude Density - Case II	6

TABLE OF CONTENTS

NONDESTRUCTIVE TESTING TECHNIQUES FOR MULTILAYER PRINTED
WIRING BOARDS

by James F. Blanche

	Page
SUMMARY	9
INTRODUCTION	9
AXIAL TRANSVERSE LAMINOGRAPHY	10
MUTUAL COUPLING	13
CONCLUSIONS AND RECOMMENDATIONS	15

LIST OF TABLES

Table	Title	Page
I.	Pickup Coil Voltages for Three Mutual Coupling Probes	14

LIST OF ILLUSTRATIONS

Figure	Title	Page
1.	Axial Transverse Laminography	10
2.	Plate I Experimental Laminograph	11
3.	Operation of the System	11
4.	Effect of Angular Variation of Main Axis	11
5.	Multilayer Test Sample	12
6.	Layer 3 of Multilayer Test Sample	12
7.	Layer 4 of Multilayer Test Sample	12
8.	Laminograph Schematic	13
9.	Principle of Operation of Mutual Coupling Probe	13
10.	Large Mutual Coupling Probe	13
11.	Comparative Sizes of Mutual Coupling Probes	14

TABLE OF CONTENTS

OPTICAL MEMORY WITH FERRIMAGNETIC STORAGE ELEMENT

by George A. Bailey

	Page
SUMMARY	17
INTRODUCTION	17
COMPENSATION POINT MEMORY	17
ELEMENT PREPARATION	19
TEMPERATURE COMPENSATION	19
BASIC MEASUREMENTS	19
CONCLUSIONS	21

LIST OF ILLUSTRATIONS

Figure	Title	Page
1.	Write and Read Cycles for Information Storage and Retrieval	17
2.	Compensation-Point Memory Construction	18
3.	Idealized Point of Coercivity Versus Temperature Variation	18
4.	Magnetization of a Typical Rare Earth (Garnet)	19
5.	Magnetization Versus Temperature of Three Gadolinium Iron Garnet Samples with Different Aluminum Doping	20
6.	Coercive Force of Gadolinium Iron Garnet	20
7.	Optical Absorption of Gadolinium Iron Garnet	20
8.	Faraday Rotation Measurement Equipment	21
9.	Faraday Rotation Versus Temperature for Two Drive Fields	21
10.	Block Diagram of Proposed System	21

TABLE OF CONTENTS

LARGE AREA METAL-OXIDE-SEMICONDUCTOR DEVICES

by Dorrance L. Anderson

	Page
SUMMARY	23
INTRODUCTION	23

TABLE OF CONTENTS (Concluded)

	Page
LARGE AREA MOS DEVICE	23
Fabrication	24
Design	25
Research Areas	26

LIST OF ILLUSTRATIONS

Figure	Title	Page
1.	Top View of Small MOS Device Prior to Wire Bonding	23
2.	Completed Large Area MOS Device	24
3.	Experimental Large Area MOS Device Ready for Diffusion	24
4.	Large Area Experimental MOS Showing Wafer Prior to Metallization	24
5.	Process Steps for Making "P" Channel MOS Transistor	25

TABLE OF CONTENTS

MICROELECTRONICS FOR THE GYRO STABILIZED PLATFORM

by Owen Rowe

	Page
SUMMARY	27
INTRODUCTION	27
DESIGN PHILOSOPHY	27
INERTIAL STABILIZED PLATFORM SYSTEM	27
MINIATURIZATION OF SPECIFIC CIRCUITS	28
CONCLUSION	31

LIST OF ILLUSTRATIONS

Figure	Title	Page
1.	Inertial Stabilized Platform System Saturn V & IB	27
2.	Gimbal Pivot Slip Ring	28
3.	Platform Servo Electronics	28

LIST OF ILLUSTRATIONS (Concluded)

Figure	Title	Page
4.	Functional Block Diagram	28
5.	AC Preamplifier, Phase Sensitive Demodulator, and Low Pass Filter	29
6.	Phase and Gain Curve Plot for the Stabilization Network	29
7.	Power Amplifier Section	30
8.	Pulse Width Modulation	30
9.	Power Bridge	30
10.	Integrated Pendulum Preamplifier	30
11.	Platform Servo Electronics (Potted and Unpotted)	30
12.	Accelerometer Output Channel	31
13.	Platform Servo Electronic Accelerator	31

TABLE OF CONTENTS

INTEGRATED CIRCUITS IN TELEMETRY SYSTEMS

by T. C. Lawson

	Page
SUMMARY	33
INTRODUCTION	33
PRESENT SYSTEM	33
NEW DEVELOPMENTS	33

LIST OF ILLUSTRATIONS

Figure	Title	Page
1.	Typical Telemetry System	33
2.	Data Compressor	34
3.	Data Compressor	34
4.	Addressable Time Division Data System	34
5.	Address System for the Addressable Time Division Data System	34
6.	Computer Interface Unit	35

LIST OF ILLUSTRATIONS (Concluded)

Figure	Title	Page
7.	Texas Instruments SNX1304 Optoelectronic Pulse Amplifier	36
8.	PCM/DDAS Model 302	36
9.	Intellux Multilayer Board	37
10.	PCM/DDAS Assembly	37
11.	Multiplexer Gates	38
12.	Printed Circuit Board Assembly	38
13.	Interconnected Printed Circuit Boards	38
14.	Electronics Chassis	39
15.	Electronics Chassis Assembly Technique	39
16.	Final Assembly	39
17.	Integrated Circuit Patch Panel (Rear View)	39
18.	Integrated Circuit Patch Panel (Front View)	40

OPTICAL ANGULAR DEVIATIONS OF 6328Å RADIATION CAUSED BY REFRACTIVE AND TURBULENT EFFECTS OF THE ATMOSPHERE

By

Robert L. Kurtz

and

James L. Hayes

SUMMARY

Atmospheric turbulence causes the image of a stationary optical source to fluctuate in intensity and position. Amplitude and frequency measurements of this random position fluctuation of the image have been made. Data were recorded over a period of approximately six months and over two different path lengths. The system and site are described. Statistical evaluation of a selected range of these data, 0 to 15 Hz, needed to determine the limitation of an experimental optical tracking system is presented and discussed.

LIST OF SYMBOLS

H	=	Horizontal
R	=	Receive
T	=	Transmit
V	=	Vertical
$\bar{\sigma}$	=	Sample mean
σ_{comp}	=	Composite standard deviation of the combined sets
σ_t	=	Rms for 0 to 15 Hertz
μ	=	Mean of composite amplitude density
μ_t	=	Mean of individual amplitude density
n	=	Number of observations
s	=	Sample standard deviation

INTRODUCTION

Turbulence between the optical transmitting point and the receiving system causes the image of that point to blur and fluctuate, both in position and intensity. This random position fluctuation of the image causes a stationary source to appear to move over a finite area with varying amplitude and frequency. The accuracy of locating this source in space is limited by the varying amplitude of the laser beam fluctuations. Measurements of these fluctuations were taken over two path lengths: case I path length of 3,200 meters and case II path length of 165 meters. The elevation angle of both paths was approximately 4 degrees with the receiving telescope approximately 2 meters above the ground level. Both paths were over varying types of terrain and ground cover. The transmission path of case I lay in a northeasterly direction, and that of case II in a westerly direction.

The magnitudes of the apparent angular deviation of the source vary with the frequency of the atmospheric fluctuations. For case I, the highest magnitudes of fluctuations occur for the frequency range 0 to 50 Hz; for case II, 0 to 10 Hz. The magnitudes of the angular fluctuations of the laser beam are reduced by a factor of at least 2, typically after 50 Hz for case I and after 10 Hz for case II. For case I, the composite rms for the 0 to 150 Hz range is approximately twice the composite rms for the range 0 to 15 Hz. For case II, the composite rms of 0 to 150 Hz is approximately 1.5 times that of 0 to 15 Hz. For a factor of 20 difference in path length of the two cases, their mean amplitude of fluctuation varied by a factor of 1.7.

Measurements of the amplitude and frequency of these apparent angular deviations of the source were recorded over a period of approximately six months under varying atmospheric conditions. The purpose of this paper is to present the results of a statistical

evaluation of a selected range of these data, 0 to 15 Hz, needed to determine the system limitation of the precision optical tracking system for advanced launch vehicles (POTSALV) being developed by this agency.

DESCRIPTION OF SIGNAL DETECTION SYSTEM AND METHOD OF SIGNAL PROCESSING

TRANSFER CURVE

An electromagnetic field around the neck of the star tracker tube of the signal detection equipment sweeps the sensitive area of the star tracker tube over the cathode in a cruciform pattern. No angular deviation (error signal) and consequently no output voltage is present when the focused laser beam is in the center of the scan pattern. As the laser beam target moves off center of the scan pattern because of increasing angular deviation, a larger output voltage is developed. This output voltage is proportional to the angle of deviation, as shown by the transfer curve in Figure 1, and is determined in the

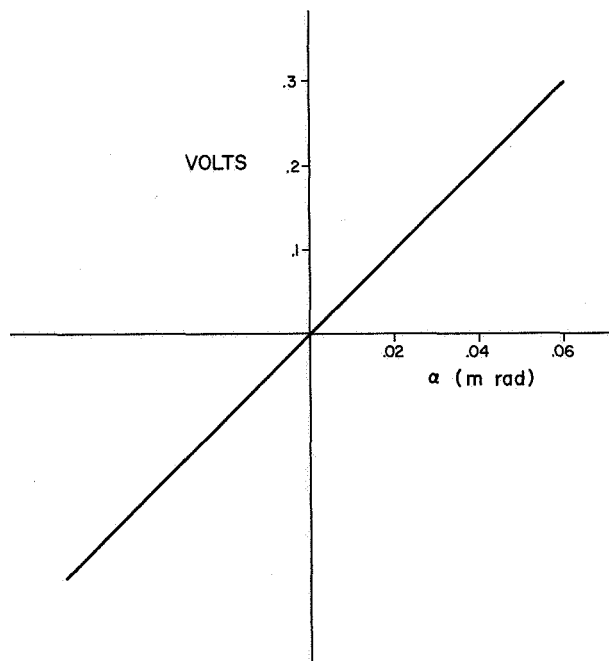


FIGURE 1. TRANSFER CURVE

following manner. The transmitting and receiving systems were placed a known distance apart. The transmitter was displaced a small distance Δd left and right of and perpendicular to the direction of

transmission. This movement produces an error signal and an output voltage which is proportional to an angle α with respect to the optical axis of the system.

SYSTEM OPERATION

A block diagram (Fig. 2) shows a remotely located laser source transmitting a 6328 angstrom beam. The laser beam with the angular deviations imposed on it is accepted by the Questar telescope. Energy from the laser beam is sharply focused onto the cathode of the star tracker tube that is electrostatically focused. An internal aperture defines a

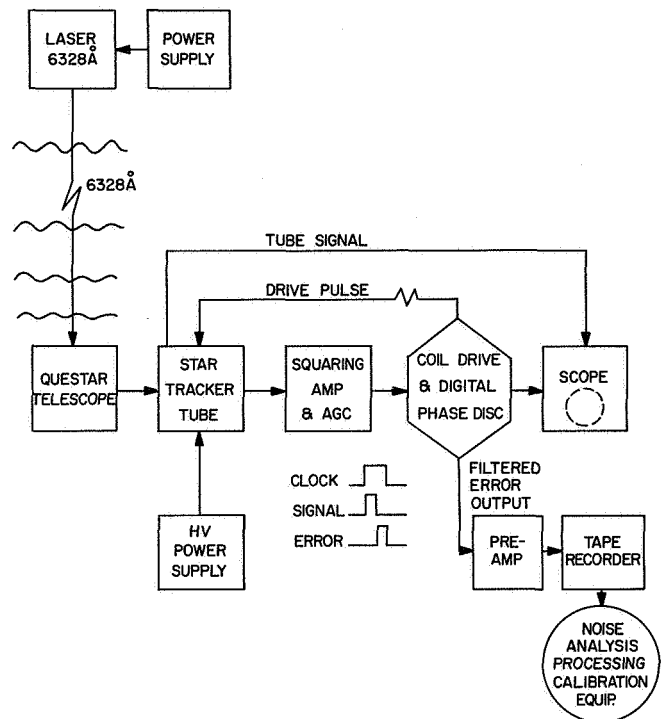


FIGURE 2. BLOCK DIAGRAM OF SIGNAL DETECTION SYSTEM

small area of sensitivity on the tube's cathode. This area is swept over a wider area of the cathode in a cruciform pattern by a quadrature magnetic field imposed by a coil around the neck of the tube. The magnitude and frequency of the apparent angular deviations of an optical source are detected as a result of the displacement of the source's image from the center of this cruciform pattern. The position of the focused spot off center of this cruciform scan pattern produces a signal which is then applied to a squaring amplifier and automatic gain control (AGC) network. On applying this output to the digital phase discriminator, the signal is phase compared to a square wave

clock pulse and an output voltage is developed. The outputs are voltages in two channels proportional to an angle taken with respect to the system's optical axis. The two channels represent angular deflections in the horizontal and vertical axes. This fluctuating output voltage is low-pass filtered from 0 to 150 Hz and recorded on magnetic tape.

SIGNAL PROCESSING

The data, recorded on magnetic tape at 19 centimeters per second (7.5 inches per second) was processed by the Noise Analysis Section of Astrionics Laboratory* A frequency spectrum analysis was performed, giving the amplitude (V_{rms}) versus frequency range of the fluctuating output voltage on the magnetic tape (2 to 150 Hz) with an effective analyzer filter bandwidth of approximately 1 Hz. The amplitude density curves are found through additional processing of the initial raw data, using the probability density analyzer.

PRESENTATION OF DATA

PROCEDURE

The apparent position fluctuation of the 6328 angstrom laser source was recorded as a fluctuating voltage on magnetic tape. Angular deviations were measured for two cases; case I has a transmission path length approximately 20 times longer than case II. The amplitude (V_{rms}) versus frequency plot of this information shows the magnitude of angular variations with frequencies of fluctuations. Amplitudes of frequencies of fluctuation up to 150 Hz were measured. The frequency region of primary interest was 0 to 15 Hz, since vehicle vibration frequencies greater than 15 Hz have negligible amplitude considering the tracking system's operation. Only this 0 to 15 Hz frequency region of primary interest is analyzed statistically. The analysis produced (1) the distribution of individual rms (σ_i) values about their mean, affording a probability prediction about the limit of rms value, and (2) the composite amplitude density distribution from individual amplitude density distributions, affording a probability prediction of limit of peak value.

DATA ANALYSIS

Case I. Data from the selected region of interest, 0 to 15 Hz, were analyzed. In this 15 Hz region, three successive 5 Hz intervals (W) were considered, producing three values of amplitude (A). These three amplitude values were used to calculate the individual rms (σ_i) of the corresponding amplitude densities.

Using

$$\sigma_i = rms = \left[\sum_i (A_i)^2 (W_i) \right]^{\frac{1}{2}} \tag{1}$$

where

A_i = amplitude

W = interval width

σ_i = rms for 0 to 15 Hz

the individual σ_i 's (rms) were calculated for all 55 runs and tabulated in order of increasing magnitude in Table I.

TABLE I. RMS VALUES FOR 0 TO 15 Hz FOR CASE I

Curve	0 to 15 Hz rms μ rad	Curve	0 to 15 Hz rms μ rad
BH6	8.4	BV14	15.5
BH11	9.1	BH2	15.6
BV5	9.2	DV2	15.7
BH7	10.1	DH1	15.8
BH9	10.3	DH6	16.1
BV3	11.9	AH2	16.2
BV9	12.0	EH2	16.4
BH4	12.5	CH2	16.8
AH4	12.6	EV1	16.8
BH12	12.7	AH1	17.0
CH3	13.0	BV8	17.1
AH5	13.2	CV3	17.1
BV13	13.2	DH2	17.1
BV11	13.3	EV3	17.3
BV4	13.4	EH1	17.7
BH5	13.4	EV2	18.4
BH8	13.6	DH7	19.0
BH3	13.8	CV1	19.4
AV1	14.2	DH4	19.6
BV2	14.4	CV4	19.9
BH10	14.4	DH5	20.9
BV6	14.8	CV2	21.0
DV1	14.8	DV3	21.0
BV10	15.0	CH1	21.9
BV1	15.2	DH3	21.9
BV7	15.2	DV4	21.9
BV12	15.5	CH4	22.0
		CV5	22.0

Explanation of curve notation: A, B, C, D, and E resulted from an attempt to group the curves by their shape. H and V are horizontal or vertical observations. For detailed information, refer to Reference 1.

* Acknowledgment is given to Messrs Heinrich Hahn, K. D. Rudolph, and Paul Martin for their work in processing this volume of data.

From the σ_i 's (rms) values of Table I a frequency histogram was prepared (Fig. 3) to present

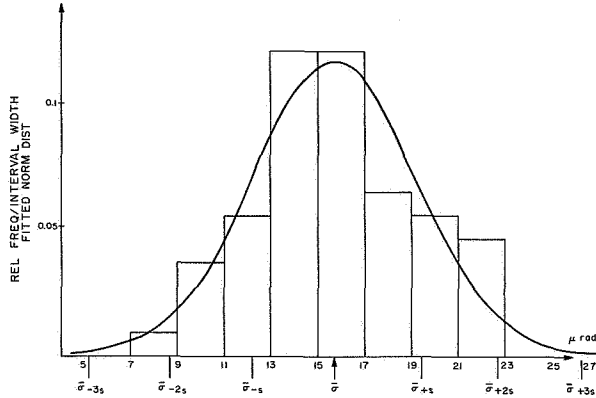


FIGURE 3. FITTED NORMAL DISTRIBUTIONS - CASE I

the combined data from the horizontal and vertical measurements. Each measurement, horizontal and vertical, is considered an independent observation. The 55 observations constitute one sample. The sample mean and sample standard deviation of this distribution were computed as follows:

$$\text{Sample mean } \bar{\sigma} = \sum_{i=1}^n \frac{\sigma_i}{n} = 15.74 \text{ microradians} \quad (2)$$

where

n = total number of samples

σ_i = rms values (Table I).

The sample standard deviation is given by:

$$s = \left[\frac{\sum_{i=1}^n (\sigma_i - \bar{\sigma})^2}{n-1} \right]^{\frac{1}{2}} = \left[\frac{\sum_{i=1}^n \sigma_i^2 - \frac{(\sum_{i=1}^n \sigma_i)^2}{n}}{n-1} \right]^{\frac{1}{2}} \quad (3)$$

and

$s = 3.51$ microradians.

Normal distribution is characterized by a skewness of 0 and a Kurtosis of 3 where

$$\text{Skewness} = \alpha = \frac{\mu_3}{s^3} = \frac{\frac{1}{n} \sum_{i=1}^n (\sigma_i - \bar{\sigma})^3}{s^3} \quad (4)$$

$$\text{Kurtosis} = \alpha_4 = \frac{\mu_4}{s^4} = \frac{1}{s^4} \frac{1}{n} \sum_{i=1}^n (\sigma_i - \bar{\sigma})^4 \quad (5)$$

where μ_3 and μ_4 are the 3d and 4th moment about the mean.

The distribution of combined horizontal and vertical data has

$$\alpha_3 = 0.15$$

and

$$\alpha_4 = 3.12$$

and therefore closely approximates normal or Gaussian distribution. A normal distribution curve was fitted to the observed data after a method by Hald [2] (Fig. 3).

Since the sample mean and sample standard deviation are not the true mean and true standard deviation, a confidence level must be placed on the rms limit. Using the tables of Bowker's and Lieberman's [3] and data of Figure 3, the probability is 0.97 that for any random sample at least 99 percent of the rms values in the sample are less than or equal to 26 microradians.

A probability prediction of the limit of peak value is afforded by the composite amplitude density distribution found in the following manner. The raw data, when processed by the probability density analyzer, produce the individual amplitude density plots for each individual observation.

From the fact that mean $\mu_i = 0$, treating each individual run as a set and using the standard deviations from Table I, a composite amplitude density distribution is found using a method by Kenny [4].

The equation for combining n sets into a single set is

$$N \sigma^2 \text{comp} = \sum_{i=1}^n k_i \sigma_i^2 + \sum_{i=1}^n k_i d_i^2 \quad (6)$$

where

$$N = \sum_{i=1}^n k_i$$

$$d_i = \mu_i - \mu$$

and

μ_i = mean of individual amplitude density

μ = mean of composite amplitude density.

For application here

$$d_i = 0 \text{ since } \mu_i = \mu = 0,$$

and $k_i = k = 1$ since we treat each run as a set of equal weight, i. e., each run represents an equal amount of sampling.

$$N = \sum_{i=1}^n k_i = nk = n = \text{number of individual sets or runs.}$$

Equation (6) becomes

$$\sigma_{\text{comp}} = \left[\frac{1}{n} \sum_{i=1}^n \sigma_i^2 \right]^{\frac{1}{2}} \quad (7)$$

where σ_i is found from Table I and σ_{comp} is the composite standard deviation or the combined sets.

Using eq. (7) and summing over the entire range of n sets yields the composite standard deviation

$$\sigma_{\text{comp}} = 16.1 \text{ microradians.}$$

This composite sigma provides the composite amplitude density distribution (Fig. 4). From this we can state that for any random sample at least 99 percent of the total time the peak amplitude of the angular deviation will be less than or equal to 48.3 microradians. In other words, for any random instant, chances are 1 in 100 for the occurrence of a peak amplitude greater than 48.3 microradians.

Case II. Raw data processed in the same manner as case I produces amplitude (V rms) versus frequency of fluctuation curves, normalized to a 1 Hz bandwidth. The measured horizontal and vertical deviations were considered independent observations and analyzed collectively in the selected region of 0 to 15 Hz.

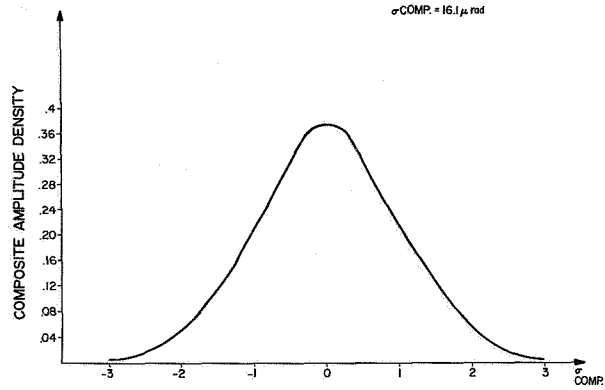


FIGURE 4. COMPOSITE AMPLITUDE DENSITY - CASE I

The individual σ (rms) for 0 to 15 Hz for each of the 52 runs is tabulated in order of increasing magnitude (Table II). From the σ (rms) values of Table

TABLE II. RMS VALUES FOR 0 TO 15 Hz FOR CASE II

Curve	0 to 15 Hz rms μrad	Curve	0 to 15 Hz rms μrad
V5	5.2	V26	8.8
H16	5.4	V18	8.9
H18	5.5	H10	9.4
H8	5.9	H21	9.5
H22	6.0	V21	9.8
H5	6.1	H25	10.0
H24	6.1	H1	10.1
V15	6.4	H3	10.1
H17	6.4	V25	10.2
H20	6.4	H23	10.4
V24	6.4	V10	10.8
H9	6.5	V13	10.8
V16	6.5	V14	10.8
V20	6.6	V3	11.0
V22	7.2	H7	11.2
H26	7.5	V19	11.5
V9	7.7	V1	11.8
H15	7.9	V4	11.8
H14	8.1	H13	12.0
V6	8.2	V17	12.0
H6	8.3	V8	12.6
H19	8.3	H11	13.2
V23	8.3	V12	13.6
H2	8.4	H12	14.0
V2	8.4	V7	14.2
H4	8.4	V11	14.6

Explanation of curve notation: A, B, C, D, and E resulted from an attempt to group the curves by their shape. H and V are horizontal or vertical observations. For detailed information, refer to Reference 1.

If a frequency histogram was prepared showing the distribution of combined horizontal and vertical measurements (Fig. 5). The 52 observations constitute one sample. The sample mean and sample standard deviation of this distribution were calculated using eq. (2, 3).

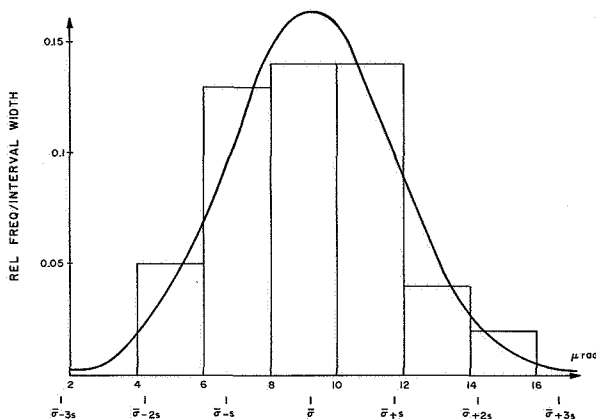


FIGURE 5. FITTED NORMAL DISTRIBUTIONS - CASE II

Sample mean = $\sigma = \sum_{i=1}^n \frac{\sigma_i}{n} = 9.19$ microradians.

Sample standard deviation = $s = \left[\frac{\sum_{i=1}^n \sigma_i^2 - \left(\sum_{i=1}^n \sigma_i \right)^2}{n} \right]^{\frac{1}{2}}$
 = 2.50 microradians.

Skewness and Kurtosis for this distribution were respectively

$\alpha_3 = .35$

$\alpha_4 = 2.01$.

Therefore, the distribution of case II is not as Gaussian as that for case I. The atmospheric process controlling optical angular deviations is known to be Gaussian. The departure of case II distribution from Gaussian is felt to be caused by the operation of heavy construction equipment in proximity to the experimental site. Evidence of this was exhibited in the data by large-amplitude low-frequency spikes, which were not present in case I data. A normal distribution curve was fitted to the observed data after a method by Hald [1] (Fig. 5).

From the data of Figure 5 and again using the tables of Bowker's and Lieberman's [2], the probability is 0.97 that for any random sample at least

99 percent of the rms values in the sample are less than or equal to 17 microradians.

A probability prediction of the limit of peak value is afforded by the composite amplitude density distribution of case II, found in the following manner. As in case I, the processed data produces the individual amplitude densities.

The processing method shows the mean $\mu_i = 0$ for individual amplitude density distribution. Using the standard deviation values of Table II and eq. (7) the composite standard deviation of the combined sets is

$$\sigma_{\text{comp}} = \left[\frac{1}{n} \sum_{i=1}^n \sigma_i^2 \right]^{\frac{1}{2}} = 9.52 \text{ microradians.}$$

This composite sigma provides the composite amplitude density plot (Fig. 6). For any random sample 99 percent of the total time the peak amplitude

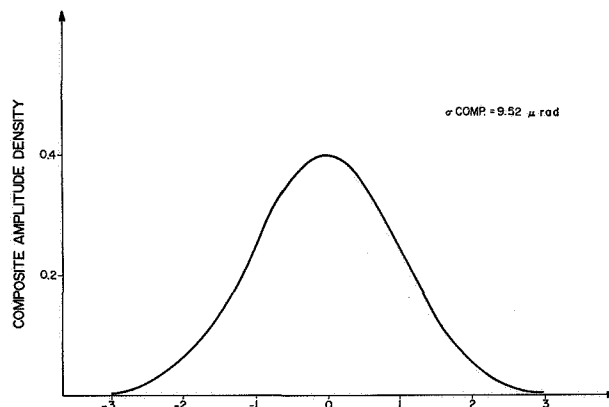


FIGURE 6. COMPOSITE AMPLITUDE DENSITY - CASE II

of the angular deviation will be less than or equal to 28.5 microradians. Thus at any random instant, chances are 1 in 100 for the occurrence of a peak amplitude greater than 28 microradians.

CONCLUSIONS

Data on atmospheric angular deviations were recorded for approximately six months and over two different path lengths. Data from each case were analyzed for the selected frequency range 0 to 15 Hz. Basic results* of the two path length measurements are tabulated as follows:

	Case I	Case II
Path length	3,200 m	165 m
Rms mean 0 to 15 Hz	15.74 μ rad	9.19 μ rad
Limiting rms 0 to 15 Hz	26 μ rad	17 μ rad
Limiting peak 0 to 15 Hz	48.3 μ rad	28.6 μ rad
<u>rms 0 to 150 Hz</u>	2	1.5
rms 0 to 15 Hz		

* For detailed information on the method of signal processing and the volume of measured data, the reader is referred to Reference 1.

REFERENCES

1. Kurtz, Robert L.; and Hayes, James L.: Optical Angular Deviations of 6328A Radiation Caused by Refractive and Turbulent Effects of the Atmosphere. NASA TN D-3439, May 1966.
2. Hald, A.: Statistical Theory with Engineering Applications. John Wiley and Sons, Inc., New York, 1960.
3. Bowker, Albert H.; and Lieberman, Gerald J.: Engineering Statistics. Prentice-Hall, Inc., New Jersey, 1961.
4. Kinney, John F.: Mathematics of Statistics. D. Van Nostrand Co. Inc., 1948.



NONDESTRUCTIVE TESTING TECHNIQUES FOR MULTILAYER PRINTED WIRING BOARDS

By

James F. Blanche

SUMMARY

A number of nondestructive testing techniques were examined as potential inspection methods for multilayer printed wiring boards. The techniques of axial transverse laminography and mutual coupling appeared most promising, and their capabilities were theoretically and experimentally verified. Axial transverse laminography is a radiographic technique that allows inspection of a thin section of a thick sample without physically sectioning the sample. It allows inspection of a conductor plane that is separated vertically from other conductor planes by as little as 0.10 mm (0.004 in.) and will detect flaws smaller than 0.02 mm (0.0007 in.). Laminography is rapid and readily lends itself to mass inspection of multilayer boards. Mutual coupling is an eddy current nondestructive testing technique that will detect a defect smaller than 0.003 mm (0.0001 in.) in the through-connection. Mutual coupling has more limitations for mass inspection than laminography because it requires probing each hole to be inspected. Application of the mutual coupling technique is envisioned as an adjunct to laminography in inspecting multilayer boards.

INTRODUCTION

One of the basic needs in the electronics field is for a high density interconnection technique that is compact, is reliable, and will eliminate the possibility of human error in wiring. Point-to-point wiring of electronic assemblies introduces the possibility for human error with every wire connected and the assembly often becomes a maze of wires. Conventional single and double sided printed circuit cards will not allow compact interconnection of microelectronic circuits. One obvious solution to this problem of high density interconnections is the multilayer printed circuit board. It allows very high interconnection density and the interconnections are identical in all assemblies using any particular circuit, so much of the possibility of human error is eliminated. However, the reliability of this system is questionable. Multilayer printed circuit boards are generally

fabricated in such a way that the internal joints formed cannot be inspected. In the most widely used multilayer system a number of copper clad sheets bonded to an insulating material are etched with the appropriate circuit pattern. The layers are laminated together and holes are drilled through the laminated assembly at the points where interlayer connections are to be made, thus exposing the edge of the copper conductors at the appropriate level. The layers are then electrically connected by plating copper onto the wall of the hole or by fusing an eyelet, tubelet, or post into the hole. Optimum interconnection is achieved when 100 percent of the surface of the hole is covered with the conducting material to a prescribed minimum thickness; and when the cylinder, thus formed, is interconnected with 100 percent of the intersecting area of the printed conductor at each layer. The problem of reliability arises in the inspection of the joints formed at the interface of the exposed edge of the printed conductors and the plated wall.

In the past, inspection has been made in several ways. One method has been to pass a high current through the joints on the theory that any poor joints will be burned out. The problem is that this stress testing may create new marginal joints. Another technique has been to check continuity of the circuitry. This method will detect opens and shorts but will tell little about the quality of the joints. Some manufacturers X-ray their multilayer circuit boards to determine how closely the layers are aligned with one another. However, an internal layer tends to be masked by the layers above it, particularly on boards with dense circuitry.

A program was initiated with the Illinois Institute of Technology Research Institute (IITRI) under contract NAS8-11288 to develop a technique to nondestructively inspect multilayer printed circuit boards. If possible, the technique was to be rapid and accurate and lend itself to mass testing. A number of techniques were examined for relative promise in fulfilling program requirements. Some of the techniques were as follows.

Techniques Involving Heat

1. Thermographic powder is applied to the surface of the board. Under ultraviolet light the

fluorescence of this powder decreases with increasing temperature and will therefore detect hot spots in the board.

2. Detection of infrared or electromagnetic radiation in the millimeter range would also detect hot spots in the board.

These techniques lose both sensitivity and resolution as the number of layers increases.

Eddy Current Techniques

Passing an ac current through a coil placed in a plated-through or eyelet hole will cause eddy current to flow in the metal on the sides of the hole. The fields of these eddy currents will in turn affect the electrical properties of the coil. By varying the frequency of the ac current and detecting the changes in the coil caused by the behavior of the eddy currents, it is possible to determine the characteristics of the joints. One of the detection systems used with the eddy current techniques was selected for more detailed study.

Intermodulation Technique

Currents of two different frequencies are passed through the printed wiring. Currents at intermodulation frequencies are then produced by any electrical nonlinearity. These intermodulation currents can easily be filtered out to detect even small nonlinearities. Attempts to detect a defect using an intermodulation technique were successful but difficulties were encountered in reproducing test results and in pinpointing the defective connection.

E-Field Sensors

Faults in printed wiring boards and plated-through holes may be found by the irregularities they cause in the equipotential surfaces of the currents flowing through the wiring. Several probing techniques to detect the irregularities were examined. These techniques are theoretically workable but there are a number of practical difficulties that would limit the usefulness of these methods.

Radiography

Neutron radiography was investigated but resolution and contrast were of insufficient quality. Autoradiography might be used if the hole plating material could be doped but the film would have to be inserted into the hole to be inspected. Electron microscopy is primarily limited to descriptions of surface characteristics. X-ray basically is limited

by the masking effect of circuit layers above the layer being inspected. The most important result of these radiographic investigations was the discovery of a technique known as axial transverse laminography which was chosen for detailed examination since it appeared to meet most of our nondestructive test requirements.

AXIAL TRANSVERSE LAMINOGRAPHY

Axial transverse laminography is a radiographic technique which allows a view of a thin section of a thick sample without physically sectioning the sample.* The technique depends on the smearing of all unwanted images over a large area while the image of interest remains sharp throughout the exposure. This result is achieved by synchronously rotating the sample and the film during exposure. The system is shown schematically in Figure 1. It consists of a point X-ray source, a rotating test table which holds the sample to be inspected, and a rotating film table. The plane that will be inspected is geometrically defined by the system. This plane is located at the intersection of the main axis and rotary axis one and will be parallel to the film plane.

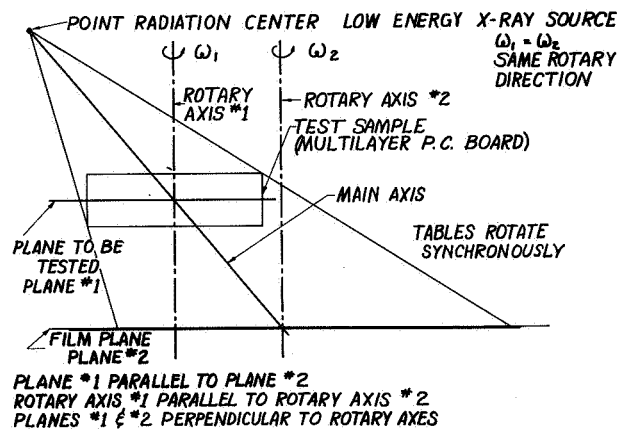


FIGURE 1. AXIAL TRANSVERSE LAMINOGRAPHY

The laboratory setup is shown in Figure 2. The low energy X-ray tube (25 keV silver K X-ray) is shown in the upper right corner. The source diameter is approximately 0.03810 mm (0.0015 in.). The grid pattern shown on the film table is for vacuum hold-down of the film. The two tables are rim driven by a single motor through rubber drive rings. Changing the compression of the rubber ring causes a variation in the driving ratio allowing precise synchronism to be achieved. The operation of the

*This technique was suggested and is being perfected by Dr. Robert Moler of IITRI. It was adapted from the systems of tomography and solidography which are used in the medical field.

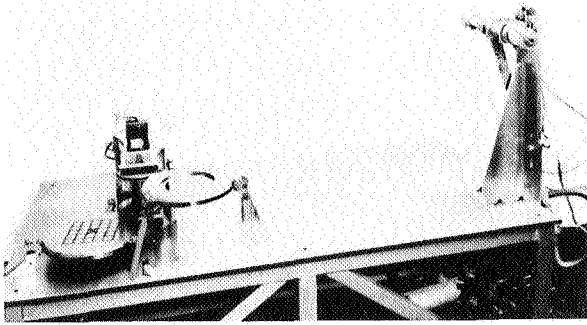


FIGURE 2. PLATE I EXPERIMENTAL LAMINOGRAPH

system is described in Figure 3. Consider line C-B to be a through-connection in a multilayer sample at

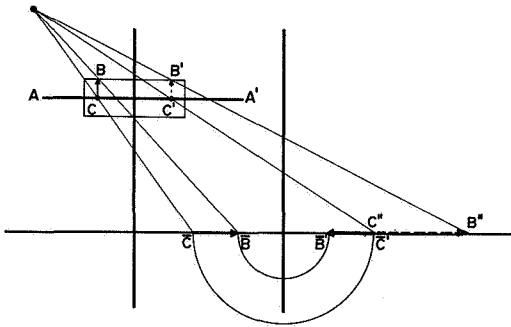


FIGURE 3. OPERATION OF THE SYSTEM

the initial point of exposure to X-ray. C-B will project $\bar{C}-\bar{B}$ onto the film. Now consider the same line C-B after it has rotated 180 degrees about rotary axis 1. The line is now defined as C'-B'. While C-B was rotating one half revolution the initial image $\bar{C}-\bar{B}$ was also rotating one half revolution about rotary axis 2 to position $\bar{C}'-\bar{B}'$. C'-B' now projects a new image C''-B'' onto the film. It will be noted that the only point where the initial ($\bar{C}'-\bar{B}'$) and the new (C''-B'') image coincide or reinforce is at point C where the sample through-connection touches the geometric plane of inspection. This example considers only two positions of the line C-B. It must be recognized that C-B is in reality projecting an image onto the film continuously throughout at least one complete revolution of the sample and film tables. Thus, it will be seen that the projected image of any point in the sample plane A-A' will reinforce itself

continuously as long as the sample and film tables are rotating synchronously, while any point outside this plane will smear out or average over a larger area. For any given vertical displacement of an object of fixed size from the plane of inspection in the sample, the area over which the object will smear is determined by the angle which the main axis makes with the horizontal plane. The angle used in the laboratory model was 20 degrees; however, a geometric analysis was performed to determine the layering sensitivity for various angles and various vertical displacements from the plane of inspection in the sample. The results of this analysis are shown in Figure 4. The curves assume a 76.2 cm (30 in.) horizontal displacement of the center of rotation of the sample from the X-ray source. Y is the vertical displacement above or below the plane of inspection of a spot 0.36 mm (0.014 in.) in diameter. The curve shows the ratio of the common area of projection of this spot to the projection of the same spot in the sample plane. It will be noted that for a vertical displacement of 0.10 mm (0.004 in.) and an angle of 20 degrees only 5 percent of the projected area of the spot is continuously reinforced or not smeared out.

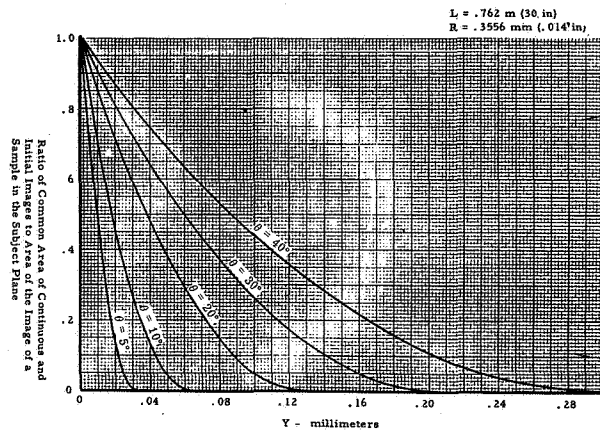


FIGURE 4. EFFECT OF ANGULAR VARIATION OF MAIN AXIS

One of the sample multilayer boards used in this program is shown in Figure 5. It is a 7 layer board with four circuit patterns. Each pattern is a hole matrix with defects built into the circuit. The patterns range from widely spaced holes to dense spacing. The most dense matrix has 100 holes or 700 joints per 6.54 cm² (1 in.²). The optimum interconnection has been defined as that where the plated cylinder makes contact with 360 degrees of the exposed conductor surface to which it is joined. Some geometric deviations were introduced into the board such as intentionally misregistering the land areas for one

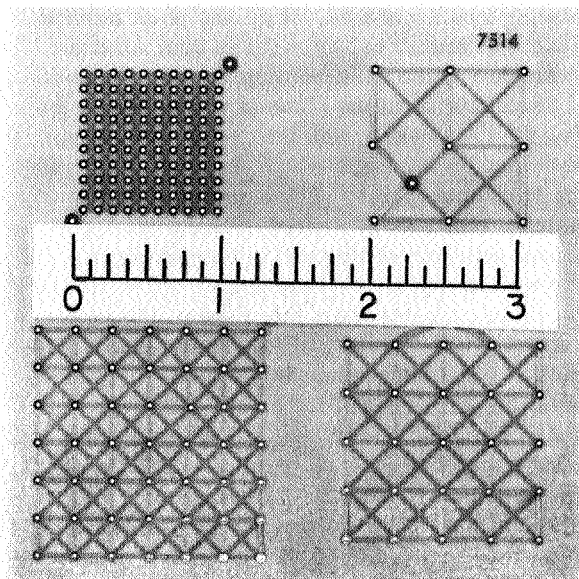


FIGURE 5. MULTILAYER TEST SAMPLE

hole in each matrix and creating open circuits by hairline fractures. The through-connections are made by plating the holes with approximately 0.004 cm (0.0015 in.) of copper. Figures 6 and 7 are laminographs of layers 3 and 4, respectively. The

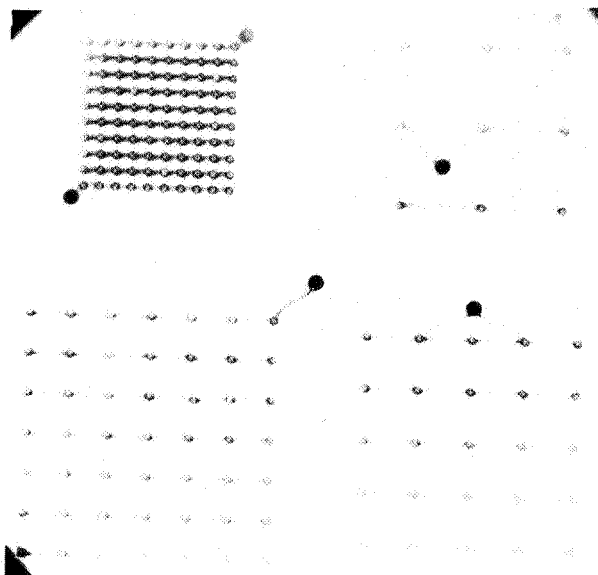


FIGURE 6. LAYER 3 OF MULTILAYER TEST SAMPLE

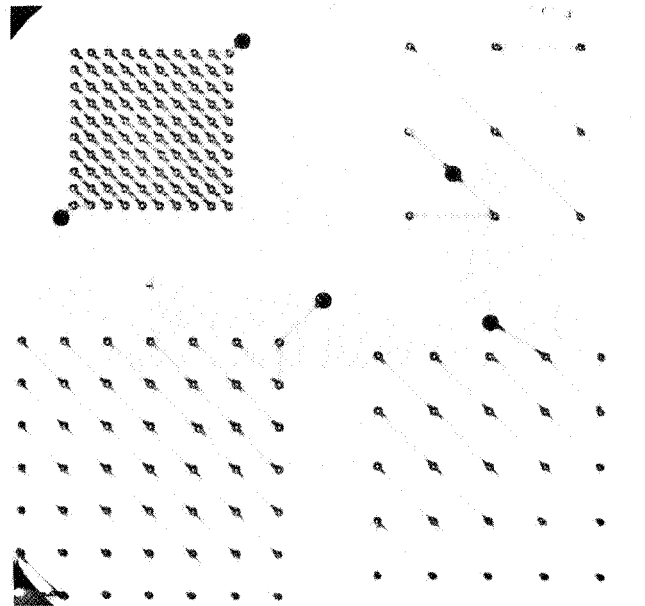


FIGURE 7. LAYER 4 OF MULTILAYER TEST SAMPLE

The two layers are separated by 0.01 cm (0.004 in.). The cuts on the diagonal line in the upper right hand pattern of layer 4 range from 37 to 88 microns wide. These laminographs have proven that the concept of axial transverse laminography is a sound one. It can separate layers at least as close together as 0.01 cm (0.004 in.) and can easily detect flaws as small as 0.02 mm (0.0007 in.).

A practical limitation is presented by the use of film. Having to take a picture of each layer and then develop and examine the film is a time consuming process. If the internal layers of the sample are not plane, several pictures of each layer may be required for complete inspection. To alleviate this problem a different approach is being taken in the laminograph now being developed by IITRI (contract NAS8-20640). Figure 8 shows the schematic. The film plate has been replaced with a fluorescent screen. The visual image from the screen is focused through a lens onto a de-rotation prism rotating at one-half the screen speed and in the opposite direction. The stationary image from the prism is projected into a closed circuit television system. The fluorescent screen will have the capability for vertical movement to change the plane of inspection in the sample. This design allows the operator to be at a remote station thus permitting safe use of higher energy, higher intensity X-ray for better resolution. The conversion to an immediate visual image of the sample produces a continuous scanning device. The operator can scan through the

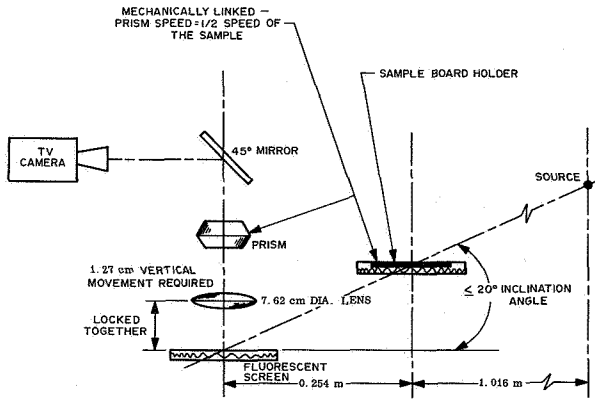


FIGURE 8. LAMINOGRAPH SCHEMATIC

complete board. A zoom attachment on the camera allows a questionable area of the sample to be magnified for more detailed inspection. Photographs of the image may be made at any time for a permanent record.

MUTUAL COUPLING

Although laminography will provide the capability to rapidly inspect multilayer printed circuit boards, the expected detail resolution of approximately 0.03 mm (0.0007 in.) may not show one serious type of defect which is an order of magnitude smaller than this. This defect is epoxy smear over the exposed surface of the internal conductors caused by improper drilling. The epoxy thus masks the internal conductors during the hole plating process and results in either an open circuit or a joint which may have far less than the desired 360 degrees of interconnection. To inspect for this condition the technique of mutual coupling has been developed. This technique uses the presence of the gap or high resistance area of the connection to develop an output signal.

The application of this technique is shown in Figure 9. Two coils wound in the form of a figure "8" are magnetically shielded from each other and formed into a single probe which is inserted into the through-hole. A signal generator is connected to one of the coils, called the excitation coil. The second coil, called the pickup coil, is shielded from the direct field of the exciting coil. When there is no gap between the plated hole and the pad, the currents that are induced in the pad circulate in the region of the pad near the exciting coil and hence induce little voltage in the pickup coil. When the probe is brought near a gap between the plated hole and the printed

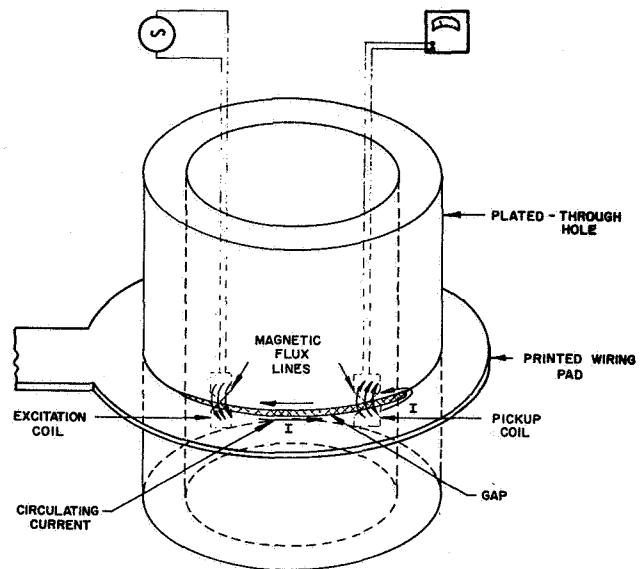


FIGURE 9. PRINCIPLE OF OPERATION OF MUTUAL COUPLING PROBE

conductor, the magnetic field from the excitation coil induces a current in the loop formed by the edge of the gap. The magnetic field from this current which circulates around the gap induces a voltage in the pickup coil. This coil is connected to a tuned voltmeter which indicates the presence of the induced voltage.

Initially a large 1.36 cm (0.85 in.) diameter probe was constructed to verify the concept (Fig. 10).

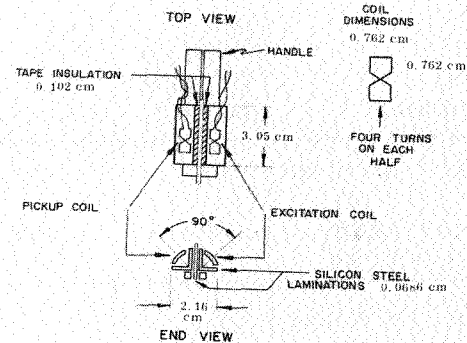


FIGURE 10. LARGE MUTUAL COUPLING PROBE

A second probe 1/10 the diameter of the initial probe was then constructed to determine the effect of miniaturization on the experimental results. When this proved successful a further reduction of 4:1 was made to produce a probe with a diameter of 0.51 mm (0.020 in.). The comparative sizes of the probes are shown in Figure 11. The results of the test run are tabulated in Table 1. In one test a bare copper

wire was wrapped around a conducting cylinder. By varying the tension on the wire a connection having low resistance but mechanically unstable characteristics was formed. The mutual coupling probe could adequately detect this type of connection.

Tests were also conducted to determine the minimum practical gap angle that could be detected. It was found that for a reasonable ratio of peak gap voltage to cylinder wall voltage of 5:1, the minimum gap angle is approximately 60 degrees. This involves rotational as well as axial motion of the probe. The probe as designed for laboratory verification of the testing technique was very delicate and is unsatisfactory for practical application. A development program on the probe is presently underway. The probe will be a single piece of electrical steel with flats on it. A layer of electrical insulation is grown on the probe and single turn figure "8" coils will be deposited on the flats. A number of coils will be deposited upon a single probe so that rotation within the hole will not be required for a complete profile. The same control tapes used in the automatic tape control drill to make the board could be used to program the probing of the plated-through holes.

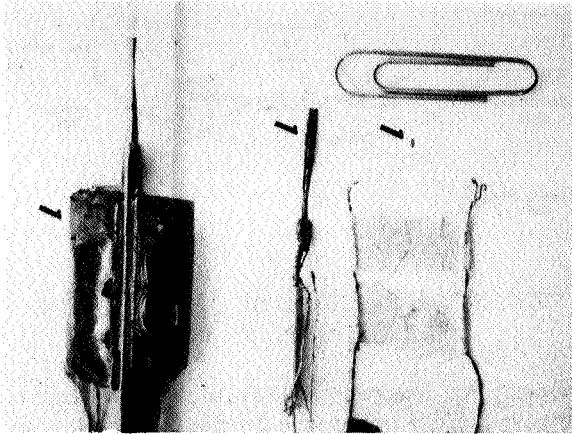


FIGURE 11. COMPARATIVE SIZES OF MUTUAL COUPLING PROBES

TABLE I. PICKUP COIL VOLTAGES FOR THREE MUTUAL COUPLING PROBES
(Excitation Current - 100 mA)

Probe Parameters	Cylinder Wall Thickness Millimeters (Inches)	Gap Width Millimeters (Inches)	Cylinder Wall Voltage, V_{cw} Microvolts	Soldered Connection Voltage, V_{sc} Microvolts	Gap Voltage, V_g Microvolts	Ratio $\frac{V_g}{V_{sc}}$
Probe Dia. = 21.59 mm (.85) freq. = 50 kHz cyl mat'l = brass	.686 (.027)	.038 (.0015)	.39	.57	15.6	27.4
Probe Dia. 2.03 mm (.080) freq. = 500 kHz cyl mat'l = copper	.102 (.004)	varied	.41	.78	4.6	5.9
Probe Dia. .51 mm (.0015) freq. = 2 MHz cyl mat'l = copper	.038 (.0015)	< .0025 (< .0001)	.12	--	1.0	8.34*

* $\frac{V_g}{V_{cw}}$

CONCLUSIONS AND RECOMMENDATIONS

Laboratory experiments have verified the feasibility of both axial transverse laminography and mutual coupling as nondestructive testing techniques for the inspection of multilayer printed circuit boards. Laminography is well suited for mass inspection of multilayer boards. It will detect flaws as small as 0.02 mm (0.0007 in.) and can distinguish conductor layers separated from adjacent layers by 0.10 mm (0.004 in.); thus it can be used for screening the boards. Work is presently underway to transform the laboratory model into a piece of practical hardware. The new system will use optical and closed circuit television techniques in conjunction with a fluorescent screen to produce a continuous scanning laminograph with the capability to make permanent records.

The application of laminography is not limited to the inspection of multilayer printed wiring boards.

It should become a powerful nondestructive testing tool for detailed examination of the interior of solid homogeneous or non-homogeneous bodies.

Mutual coupling can be used as an adjunct to laminography in the detection of extremely small gaps in the through-connections, but it is more limited in application because it requires probing each through-connection to be inspected. The laboratory model of the 0.51 mm (0.020 in.) diameter probe was difficult to fabricate and was too fragile to be practical. Work is being done to deposit 4 to 6 coils on a single probe to simplify the probing operation, to improve the geometry of the probe, and to reduce the minimum gap angle that can be detected. While these two complementary techniques will not answer all the questions concerning the quality of multilayer wiring boards, they will go a long way toward answering the question of reliability of the interconnections.



OPTICAL MEMORY WITH FERRIMAGNETIC STORAGE ELEMENT

By

George A. Bailey

SUMMARY

A fifteen month effort to fabricate a magneto-optic memory is summarized. The scope of work included efforts to produce a material that would operate at room temperature without compensation. The material was evaluated to determine its magnetic, optical, and thermal properties such that the design of the memory might be optimized. To demonstrate the results of the experimentation, a feasibility model was designed and fabricated.

The storage element chosen was gadolinium iron garnet doped with aluminum. Information is written into the memory by simultaneously applying heat and a magnetic field to a spot. Since the coercivity of the material is temperature dependent, only the heated portion of the garnet is affected by the field. The readout signal is derived from the Faraday rotation of a polarized beam of light by the element. The state of magnetization of a region is determined by observing the direction of Faraday rotation.

INTRODUCTION

It is generally recognized that for large random access systems (greater than 10^6 words) the most debilitating influence on the system comes not from the memory element, but from the peripheral interconnections and equipment. The optimum system would require the highest degree of reliability.

One technique to eliminate the large numbers of access interconnections is to use optics. With proper techniques a beam of light may be steered randomly to any point within a memory matrix. This eliminates the large logic decoding trees with the attendant drive lines. Optical access memories have been devised using the Kerr effect, but the writing functions must still be line driven. Memories have been proposed using holographic and photochromic devices; however, they have not progressed much past the conceptual stage of development. On the other hand, the ferrimagnetic memory is both written and read optically; thus, it has greater potential for mass memory application.

COMPENSATION POINT MEMORY

The storage element used is a gadolinium iron garnet, which exhibits the necessary ferrimagnetic properties; that is, the magnetic moments of gadolinium and iron align in opposition, and the magnitude of the moments is temperature dependent. The resultant magnetic moment of the element is the difference between these two sublattice moments. At a particular temperature the magnetic moments of gadolinium and iron are equal and opposite, thereby cancelling each other. This temperature is called the compensation temperature or compensation point.

At the compensation point there is no net magnetic moment; therefore, the element is unaffected by external magnetic fields. Since the magnetic moments of gadolinium and iron exactly cancel, no further reduction in energy would be accomplished by the application of a field. This point is illustrated in Figure 1. The memory described below operates around this compensation point.

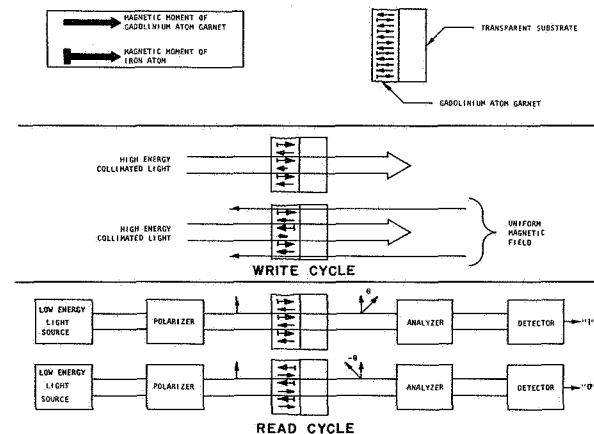


FIGURE 1. WRITE AND READ CYCLES FOR INFORMATION STORAGE AND RETRIEVAL

The construction of the compensation point memory is shown in Figure 2. The memory element is a thin slab of ferrimagnetic material which is held at its compensation temperature. The magnetic

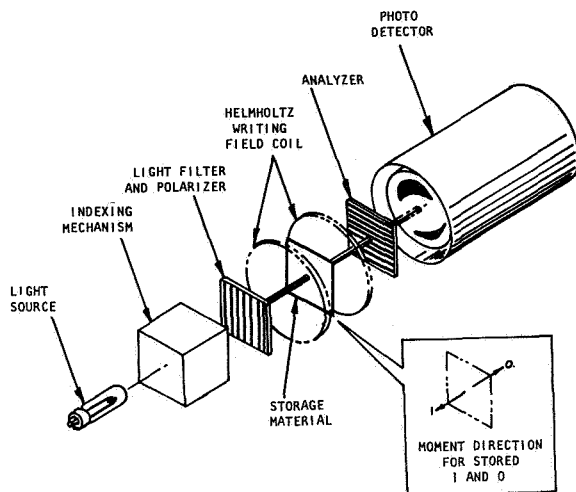


FIGURE 2. COMPENSATION-POINT MEMORY CONSTRUCTION

easy axis is normal to the slab. Writing is accomplished by heating a local area to reduce the coercivity and then applying a magnetic write field to set the memory. The write field is applied by a single Helmholtz coil. The magnitude of the field is much lower than the coercivity at the compensation temperature, but is greater than the coercivity in the heated area. Consequently, only the magnetic moment in the heated area is oriented in the direction of the applied field. Reading is accomplished by applying a beam of polarized light to the spot to be read. The transmitted light is passed through an analyzer and detected by a phototube. Because of the Faraday effect, the plane of polarization of the incident light is rotated as it passes through the magnetic medium. The rotation of the plane of polarization is clockwise or counterclockwise depending upon whether the magnetization is parallel or anti-parallel to the beam of light. One direction is defined as binary 1, the other as binary 0. Consequently, a stored 1 can be distinguished from a stored 0 by observing the amplitude of the transmitted light. The readout is, obviously, nondestructive.

The write cycle time depends on the thermal relaxation time of the memory element, the temperature change required to take the element from a non-disturb to write state, and the magnitude of the write field. The variation of coercivity with temperature about a compensation point is shown in Figure 3. To write into the memory, the temperature of the selected bit must be raised to at least T_r , such that a write field of H_w may operate on the spot,

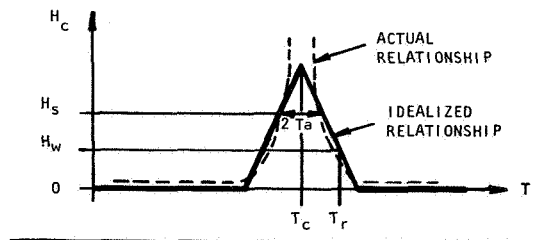


FIGURE 3. IDEALIZED POINT OF COERCIVITY VERSUS TEMPERATURE VARIATION

and then reduced to $T_c + T_A$ before the write field can be removed. Thus, the write cycle consists of selecting a spot, raising, and then lowering its temperature in the presence of a field. The cycle time depends upon how fast these operations can be performed. The writing time can be reduced by increasing the power of the heating pulse. The time required to lower the temperature will depend upon the thermal relaxation time constant of the material.

The material required for a fast-write-cycle memory should have an H_C versus T relationship with the general shape of that shown in Figure 3. The effective sheet coercivity, H_s , should be as high as possible for the specified variation in ambient temperature, T_C , and the slope of the curve should be as steep as possible. The material should have a large thermal conduction coefficient; or preferably, it should be prepared on a transparent substrate with a large thermal conduction and large specific heat. Since the element is heated by a beam of light, the storage element should be sufficiently opaque to absorb energy and sufficiently transparent to be heated internally.

The read operation is based on the use of polarized light and the Faraday effect. A large rotation of the plane of polarization of the read light beam is desired to improve the discrimination between 1 and 0 outputs and to relieve the requirements on the analyzer. Since the magnitude of the rotation is proportional to the thickness, thick elements are seemingly preferred. However, absorption of the light implies that thin samples are desirable. A figure of merit is the ratio of the rotation power to the absorption coefficient. Thickness considerations impose practical limitations on the choices for light sources and detectors. The read cycle time is determined primarily by the indexing time and the detector speed.

Since no switching is involved in the read operation, the time delay in the storage medium is negligible.

ELEMENT PREPARATION

Three primary methods of preparing the gadolinium iron garnet were investigated: thin films, polycrystalline samples and single crystals. The results of the thin films were disappointing. Polycrystalline materials were obtained and found to be quite comparable in optical absorption and Faraday rotation to the single crystal material. However, polycrystalline samples could not be made as thin as the single crystal material and the polycrystalline material did not exhibit magnetic anisotropy. Therefore, the direction perpendicular to the plane of the element could not be made into an easy direction. Single crystal material was prepared by the molten flux method.

TEMPERATURE COMPENSATION

In the gadolinium iron garnet, $Gd_3Fe_5O_{12}$, the iron ions occupy two different sites. Three of the atoms in the unit cell occupy tetrahedral sites, and the other two occupy octahedral sites. The iron atoms in the octahedral and tetrahedral sites are coupled antiferromagnetically. The resultant magnetization of the iron atoms is coincident with the iron atoms in the tetrahedral sites.

The gadolinium ions are coupled antiferromagnetically to the net moment of the iron ions. The coupling is much weaker than that between the iron ions. As a consequence the magnetization of the gadolinium ions drops very quickly with increasing temperature, approximately as $1/T$. Therefore, at temperatures near the curie point, the magnetization of the iron ions is dominant. However, since the gadolinium has a saturation moment larger than the resultant magnetization of the iron ions, the moment of the gadolinium ions is predominant at low temperatures. The temperature at which the gadolinium and iron magnetic moments are equal is called the compensation point.

Figure 4 shows a plot of the magnetization of the iron ions and the gadolinium ions as a function of temperature. The total magnetization is also shown. At the temperature marked, T_c , the magnetization of the gadolinium and iron ions cancels.

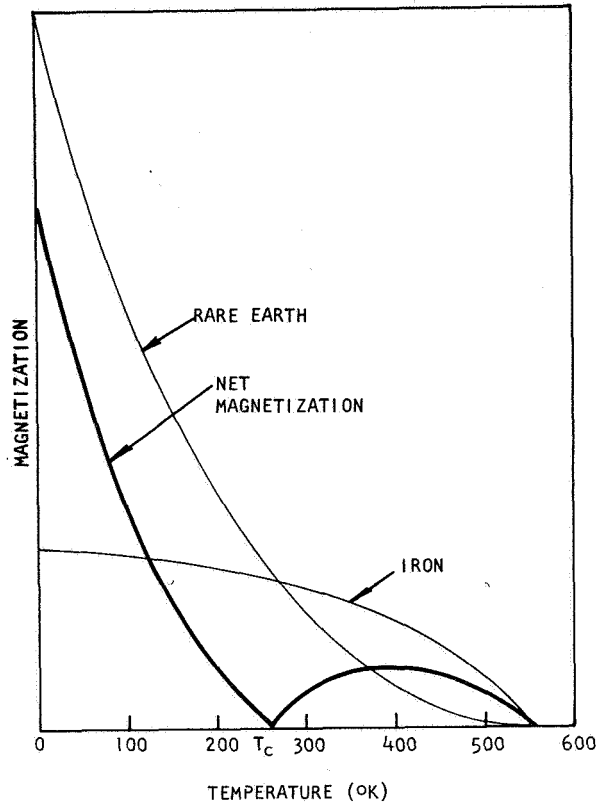


FIGURE 4. MAGNETIZATION OF A TYPICAL RARE EARTH (GARNET)

The compensation temperature of gadolinium iron garnet is $288^{\circ}K$. The substitution of aluminum for the iron reduces the moment of the iron lattice. The aluminum preferentially occupies the tetrahedral sites because the aluminum atom is smaller than the iron atom and also the tetrahedral sites are smaller than the octahedral sites. A reduction in the net magnetization of the iron lattice raises the temperature at which the iron lattice is compensated by the gadolinium lattice. This program dictated a memory which could operate at room temperature without compensation. It was found that four percent by volume of aluminum substituted for the iron resulted in crystals with a compensation temperature very close to room temperature.

BASIC MEASUREMENTS

To design a memory based on gadolinium aluminum iron garnet, measurements of certain magnetic and optical properties of the material are essential. Both the compensation temperature and the coercivity were determined with the aid of a vibrating magnetometer; a sample is vibrated in a dc magnetic field, and the

magnetization is sensed with a pick-up coil. Figure 5 illustrates plots of magnetization versus temperature of three different samples. The temperature at

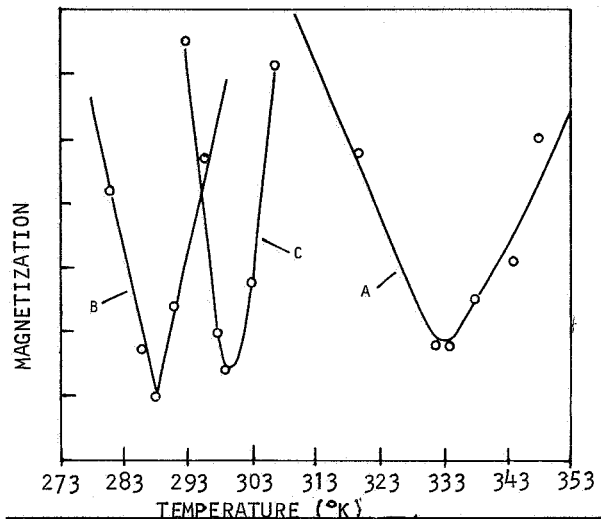


FIGURE 5. MAGNETIZATION VERSUS TEMPERATURE OF THREE GADOLINIUM IRON GARNET SAMPLES WITH DIFFERENT ALUMINUM DOPING

which the magnetization is minimum is the compensation point. Reversing the dc field and noting the reversal of magnetization gives the value of the coercive force. A typical plot is shown in Figure 6.

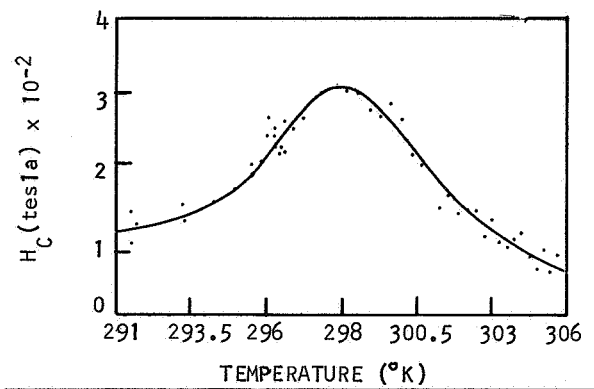


FIGURE 6. COERCIVE FORCE OF GADOLINIUM IRON GARNET

These results indicate the temperature stability of the memory. For example, to write into the memory by heating a bit 6°K above the compensation temperature, a field of 7843 amperes per meter (100 oersteds) would be needed to switch the heated area. This field would not affect the unheated portion of the platelet as long as the temperature is maintained within 6°K of the compensation temperature. The sharper the peak, the easier the writing; however, a sharp peak requires better temperature stability.

The optical absorption measurements were obtained with a spectrophotometer. A typical run is shown in Figure 7. The optimum wavelength is one

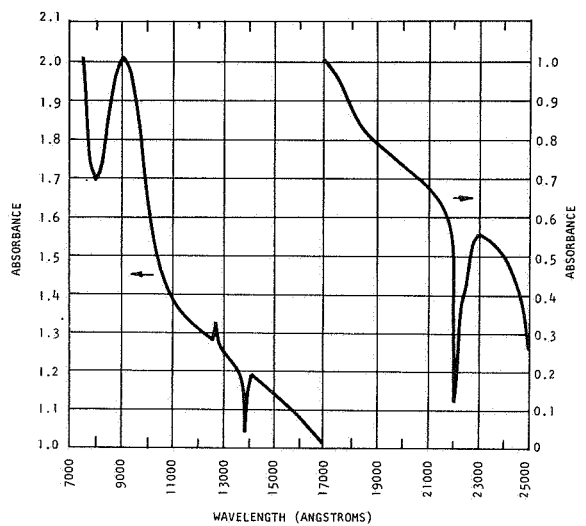


FIGURE 7. OPTICAL ABSORPTION OF GADOLINIUM IRON GARNET

that has the largest rotation of polarization per loss by absorption. These results indicate that, if the Faraday rotation is not significantly reduced, the longer wavelengths are more desirable.

Faraday rotation measurements were obtained with the aid of the arrangement shown in Figure 8. The laser beam was modulated at 90 Hz, passed through a polarizer, the sample, and an analyzer, and then detected by a photomultiplier. The laser beam was also detected by a phototransistor and this signal in the differential amplifier. The results of a typical set of measurements are shown in Figure 9.

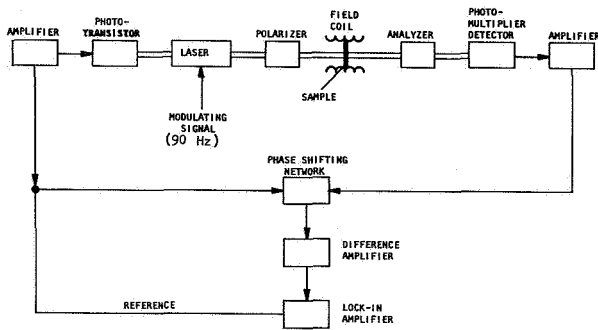


FIGURE 8. FARADAY ROTATION MEASUREMENT EQUIPMENT

From these curves it is evident that the temperature stability depends upon the magnetic field used for writing. With a field of 784 amperes per meter (10 oersteds), no rotation occurs over a range of above 6°K. For a 1500 amperes per meter (20 oersted) field, the temperature range over which no rotation occurred was reduced to about 3°K.

CONCLUSIONS

Based on the experimental information, a feasibility model of the concept has been designed and fabricated. A block diagram of the system is illustrated in Figure 10. The memory elements are on 25 micron (1 mil) centers that probably can be reduced to 2.5 micron (0.1 mil) centers. With an

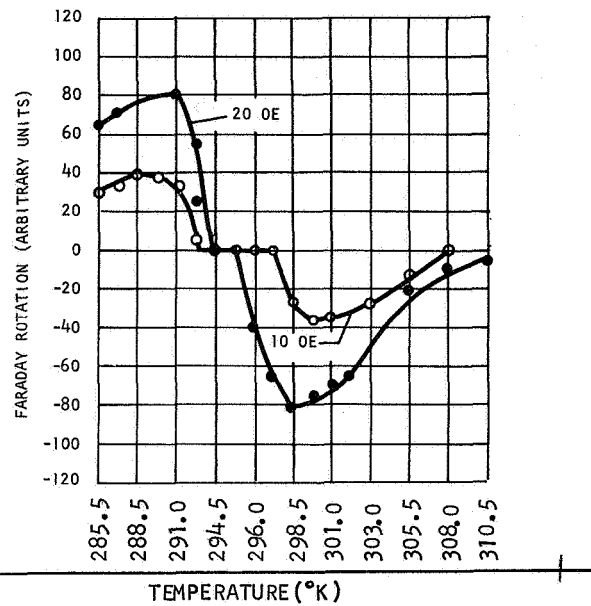


FIGURE 9. FARADAY ROTATION VERSUS TEMPERATURE FOR TWO DRIVE FIELDS

argon laser, Faraday rotations of 9 degrees are obtained, therefore detection is no problem. The small memory elements have greatly enhanced the cycle times of the memory. Since the beam from the laser could not be reduced to this micron range, a special diffraction-limited focusing lens had to be used. The present major difficulty is securing some type of non-mechanical laser scanning apparatus. Various techniques have been proposed; for example, modulating

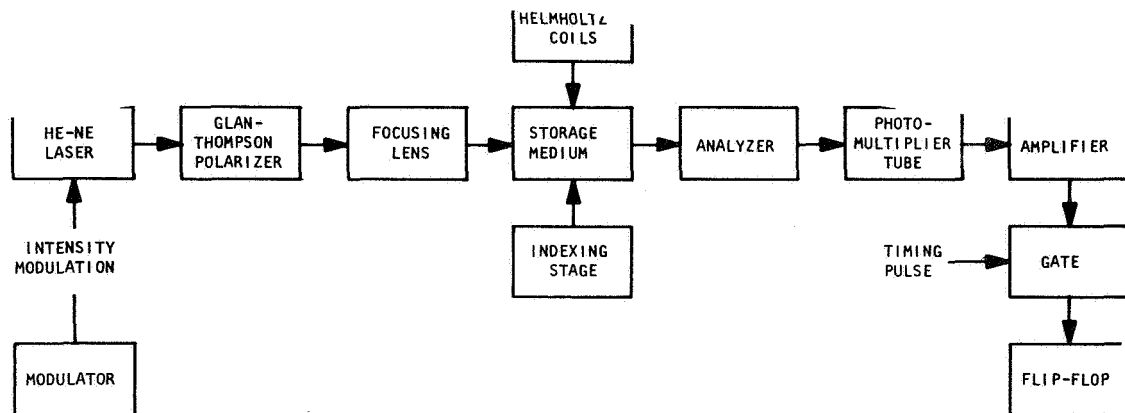


FIGURE 10. BLOCK DIAGRAM OF PROPOSED SYSTEM

GEORGE A. BAILEY

the index of refraction of crystals, employing standing waves in crystals, and revolving mirrors on the end of a turbine dentist's drill. All of these ideas are basically mechanical operations and are, therefore, limited in speed. The technique offering the most promise is the combination of potassium

dihydrogen phosphate and calcite arrangement that can be driven by digital signals. Overall, this system promises a 10^8 bit memory on a 6.5 square centimeter (one square inch) substrate which can be randomly accessed without hard line interconnections.

LARGE AREA METAL-OXIDE-SEMICONDUCTOR DEVICES

By

Dorrance L. Anderson

SUMMARY

The Solid State Devices Section at MSFC has followed the development of metal-oxide-semiconductor (MOS) devices for several years. Interest in this field stems from its importance in several electronic applications. A large area MOS transistor is being developed for incorporation in an integrated circuit and for studying certain problems in fabricating MOS devices.

This paper describes the design and development of a "P" channel MOS transistor with a channel width of 1.8 centimeters. Calculations are made on drain to source current, input capacity, and transconductance.

Areas for research in MOS structures are discussed with particular interest being placed on materials and techniques that promise improvements attainable in the near future. Semiconductors, dielectrics, and metal systems are discussed separately with possible direction for fruitful research in each.

INTRODUCTION

Rapid advances are now being made in metal-oxide-semiconductor (MOS) technology as a result of increased development efforts and funds being expended. Some advantages offered by MOS devices and circuits are small size, low power consumption, simple construction, high yield, and high input impedance with an output characteristic similar to that of a pentode vacuum tube.

Although there will be some uses for individual MOS devices, the greatest use will be in large scale integration of many functions into a single chip. Because of high yields and small size, very complex arrays are possible.

A program to develop an MOS device having a large area was to have resulted in an MOS technology

capability and a transistor for use in a special circuit. Because of the large size and channel width, fabrication of the transistor proved to be difficult. The design and fabrication of the device are described below.

LARGE AREA MOS DEVICE

A "P" channel enhancement mode transistor with a current capacity of approximately one-fourth ampere was desired. Silicon was used as the semiconductor material, thermally grown silicon dioxide formed the gate dielectric, and aluminum served as the metal contacts. Since current rating and transconductance depend on channel width, an interdigitated structure was designed for greater channel width per given surface area. A small experimental MOS device with a 15 micron channel length and a 25 micron channel width is shown in Figure 1. The solid aluminum

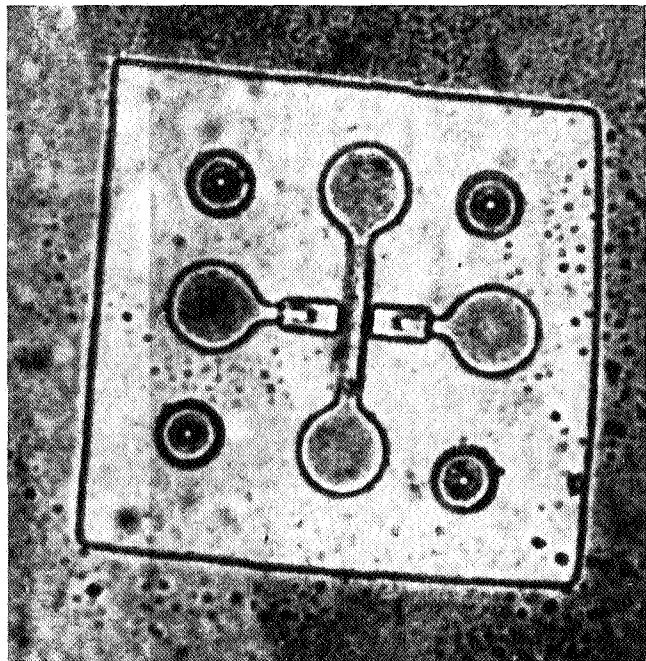


FIGURE 1. TOP VIEW OF SMALL MOS DEVICE PRIOR TO WIRE BONDING

stripe with a pad on each end is the gate metallization over the channel. Figure 2 shows the large area

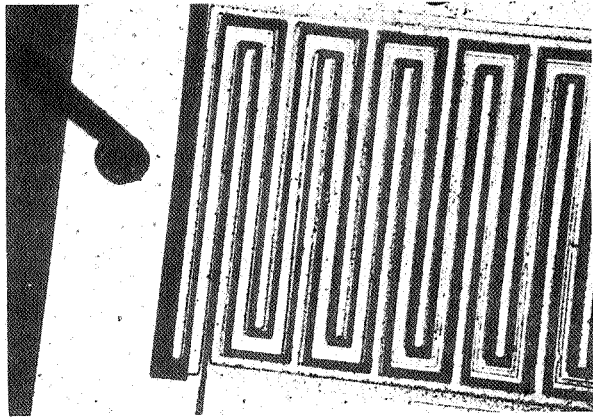


FIGURE 2. COMPLETED LARGE AREA MOS DEVICE

device with the same channel length of 15 microns but with a channel width of approximately 1.8 centimeters. Figure 3 shows the wafer just before diffusion of source and drain; the light areas are the openings in the oxide with the silicon exposed.

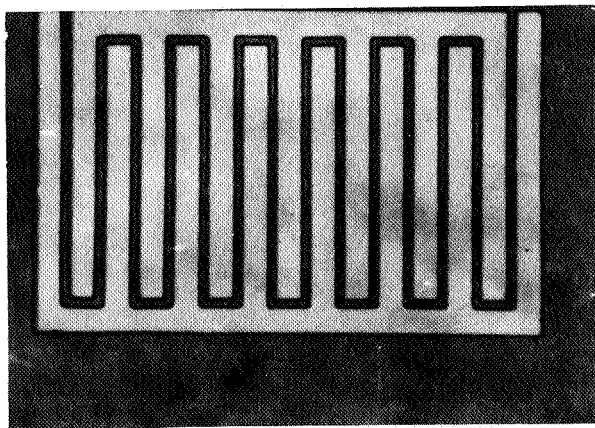


FIGURE 3. EXPERIMENTAL LARGE AREA MOS DEVICE READY FOR DIFFUSION

4 was taken just before the aluminum pattern was applied; the light areas are the exposed silicon in the source and drain regions, the dark areas are silicon dioxide, and the medium zigzag stripe is the thinner oxide over the channel.

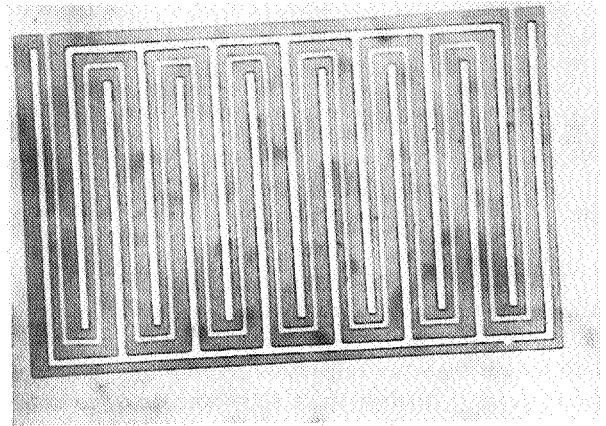


FIGURE 4. LARGE AREA EXPERIMENTAL MOS SHOWING WAFER PRIOR TO METALLIZATION

FABRICATION

A detailed step-by-step breakdown of the fabrication process is shown in Figure 5. The following is a description of these steps:

1. An N-type wafer of 6 to 7 ohm centimeters was chosen. The wafer had previously been lapped and chemically etched. The wafer was cleaned in ethyl alcohol and dried under a sun lamp for 15 minutes.
2. An oxide of 4500 angstroms was thermally grown in an open tube furnace at a temperature of 1373° K. The first 15 minutes of growth was in dry oxygen. This was followed by one hour in steam and finished with 15 minutes in dry nitrogen.
3. After oxidation, the wafer is placed on a spinner and photoresist is applied. The photoresist is air dried for 15 seconds and spun at 10 000 rpm for 30 seconds, resulting in a uniform coating. It is then placed in an oven and baked 40 minutes at 333° K.
4. The photoresist is exposed by aligning a previously prepared photographic mask over the wafer and exposing it to ultraviolet light for one minute. The wafer is then placed in an oven at 453° K for 30 minutes to cure the photoresist before oxide etch.
5. The exposed oxide is etched down to the silicon with a buffered solution of hydrofluoric acid containing acetic acid, ammonium fluoride and de-ionized water.
6. The polymerized resist is removed with boiling j100-strip solution.

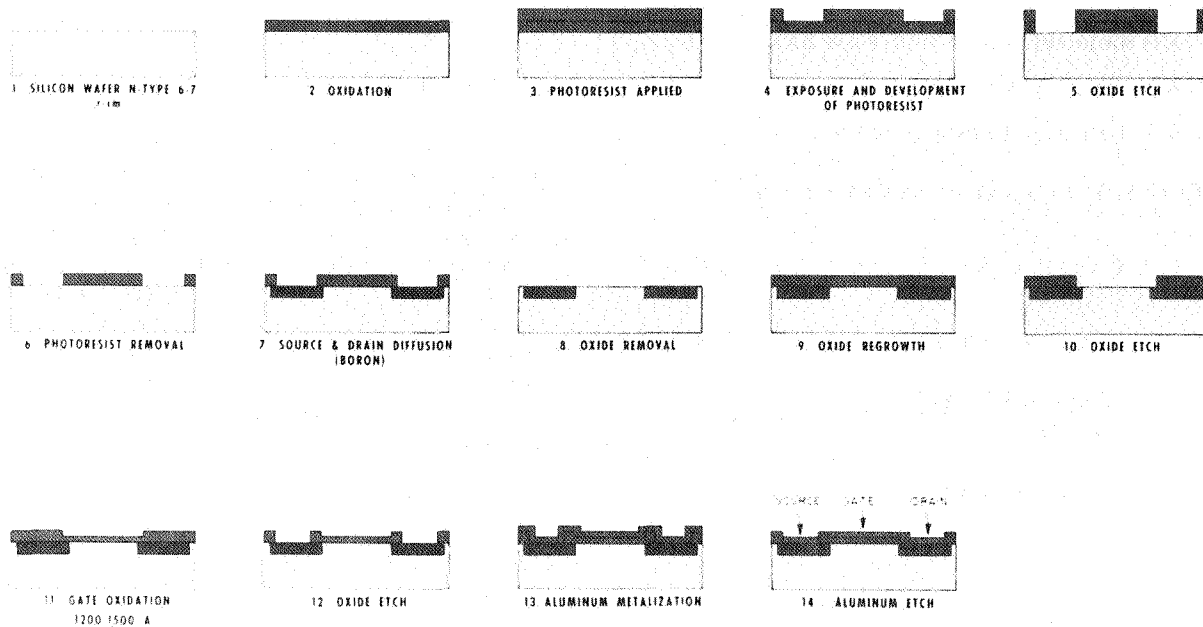


FIGURE 5. PROCESS STEPS FOR MAKING "P" CHANNEL MOS TRANSISTOR

7. Source and drain diffusion are made in an open tube furnace at 1473°K. A gas system is used with diborane as the dopant and argon as the carrier. Diffusion time is approximately 40 minutes and depth of diffusion 4 microns.

8. Because of doping impurities in the oxide, it is stripped from the entire wafer with the buffered etch solution used in step 5.

9. A new oxide is regrown by the same process used in step 2.

10. To obtain a thin layer of oxide over the channel between source and drain, the oxide is etched down to the silicon.

11. An oxide 2000 angstroms thick is grown over the channel in dry oxygen at 1373°K for 45 minutes. It is easier to grow a 2000 angstrom oxide than to etch back from a thicker one.

12. Oxide is removed from source and drain areas for metallization contacts. The etch is the same used in step 5.

13. The entire surface of the wafer is coated with aluminum by vapor deposition. This is accomplished in a vacuum system at 1.3×10^{-4} newtons per square meter (10^{-6} torr).

14. Aluminum is removed from the entire wafer except over the gate region, source and drain contact areas, and contact pads. This is accomplished by using photo-engraving techniques previously described and a buffered solution of phosphoric acid, nitric acid, and deionized water.

The wafer is now ready for dicing and mounting of the individual chips on headers.

DESIGN

To determine the current capacity per centimeter of channel width, the following formula was used:

$$I_{ds} = \frac{\mu_0 C_i V_g}{2l}$$

where

$$\mu_0 = 250 = \text{hole mobility}$$

$$C_i = \text{capacity/cm}^2$$

$$V_g = \text{gate voltage}$$

$$l = \text{channel length in cm}$$

$$C_i = 0.08842 K \frac{A}{d} \mu\mu F$$

DORRANCE L. ANDERSON

where

K = dielectric const. = 3.8 for SiO_2

A = area in cm^2

d = dielectric thickness in cm .

With an SiO_2 thickness of 2000 angstroms

$$C_i = 0.08842 (3.8) \frac{1}{2 \times 10^{-5}} = 0.0168 \mu\text{F}/\text{cm}^2.$$

With $V_g = 1$ volt and channel length of 15 microns

$$I_{ds} = \frac{250 (.0168 \times 10^{-6})}{2 (15 \times 10^{-4})} = 1.4 \text{ mA}/\text{cm} .$$

With a gate voltage of 10

$$I_{ds} = 10^2 \times 1.40 = 140 \text{ mA}$$

for a 0.25 A device

$$250/140 = 1.8 \text{ cm channel width required.}$$

Transconductance per cm of channel width at $V_g = 1\text{V}$

$$g_m = \frac{\mu_0 C_i V_g}{l}$$
$$= \frac{250 (.0168) 1}{15 \times 10^{-4}} = 2800 \mu \text{ mho}/\text{cm}$$

or $1.8 \times 2800 = 5000 \mu \text{ mho}$ for the device

at $V_g = 10$ volts, $g_m = 50,000 \mu \text{ mho}$.

Although the values measured on completed devices were not as high as the theoretical values, the results were satisfactory for the application. Development is continuing on MOS devices with special emphasis on oxide growing. Oxides will be grown at temperatures around 1273°K under various conditions of gas flow to minimize immobile charge density.

This should reduce threshold voltages, which were excessively high in the devices fabricated to date.

RESEARCH AREAS

Because of the vast amount of existing knowledge in bipolar planar technology, the development of MOS devices has largely used the same materials and techniques. The MOS transistor, however, operates on an entirely different principle and a new look should be taken at promising semiconductor materials. Gallium arsenide, for instance, has higher mobility and offers the promise of higher speed devices. A study to compare various semiconductor materials for specific use in MOS devices could prove very beneficial.

Although thermally grown SiO_2 has spawned the planar technology and consequently the integrated circuit industry, it still is not the ideal masking and insulating agent. Neither is it the ideal dielectric for the gate of an MOS transistor. Silicon nitride is denser, has a higher dielectric constant, and has shown signs of making devices more stable under temperature and radiation environments. Silicon nitride is more difficult to etch than silicon dioxide, and efforts are now concentrated on window cutting techniques to use silicon nitride in mass production.

Another interesting approach to field effect devices is replacing the dielectric with ferroelectric materials. Then by applying a potential to the gate, a channel can be enhanced or depleted by voltage pulses. This has the requirements of a memory cell.

The possibilities for research in gate insulating materials are almost unlimited. This is probably the most fruitful area in MOS research.

In general the surface has only been scratched in MOS technology. The field is wide open for research in semiconductors, dielectrics, and metals as applied to field effect devices.

MICROELECTRONICS FOR THE GYRO STABILIZED PLATFORM

By

Owen Rowe

SUMMARY

The microminiaturization of the gas bearing gyro servoloop electronics and associated circuitry for the platform are discussed. Emphasis is placed on the redesign of the electronics to achieve maximum monolithic integration. A number of circuits are presented to demonstrate the achievements. Evidence is shown that linear-analog circuits can be miniaturized with corresponding benefits.

INTRODUCTION

For several reasons, the stabilized-platform electronics were built with large elements. The circuits were the linear-analog type and were designed to handle large dynamic signal levels and high power output. Long time constants are involved in operating the gyro, and precise specifications must be met; therefore, the circuits could not easily be miniaturized. Also, the semiconductor industry waited to develop the required circuitry because of their concentration on digital circuits.

Approximately two years ago, a serious effort was started to miniaturize the platform electronics. With increased reliability as the main objective, an appraisal of miniaturization techniques was made. The decision was to design for maximum use of the monolithic integrated chips. Some forms of hybrid circuitry using the deposited films and discrete components were more advanced, but they did not show as high a reliability potential. The hybrid approaches involved too many interconnections of dissimilar materials. The design approach using the monolithic integrated chips depended upon further development of standard as well as custom integrated circuits.

DESIGN PHILOSOPHY

It was evident that extensive circuit redesign was required for microminiaturization. First the large elements such as transformers, reactors and large capacitors had to be eliminated. These elements

comprised approximately two-thirds of the volume and weight. Secondly, the power dissipation in the circuits had to be reduced to avoid the massive heat sinks. The circuits also had to be designed for long time constants, freedom from ground loops, immunity to noise and cross-talk, good linearity, and low-null drift or good dc stability. To obtain these goals with integrated circuits required new concepts in circuit design philosophy. Previously, with discrete elements, a minimum number of transistors were used along with the large elements to obtain a given circuit function. In monolithic chips, transistors are a real bargain, and many transistors should be used to the exclusion of large elements.

INERTIAL STABILIZED PLATFORM SYSTEM

Figure 1 shows the four major assemblies that make up the platform system. The system functions

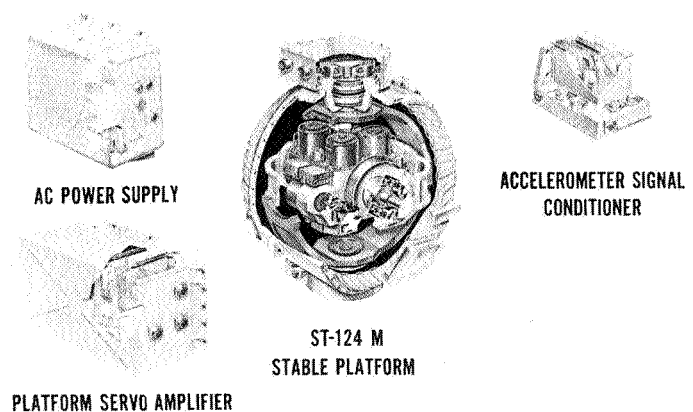


FIGURE 1. INERTIAL STABILIZED PLATFORM SYSTEM SATURN V & IB

are (1) accelerometer sensing and reference, (2) vehicle attitude and programming, and (3) guidance reference coordinates. The stable platform assembly contains the inertial sensors and the associated gimbals. The ac power supply is a static inverter for converting battery power to 3 phase 400 Hz to drive the gyro wheels and to supply other reference voltages. The servoamplifier box contains six sets

of servoelectronics and miscellaneous control circuitry. The accelerometer signal conditioner contains the wave shaping amplifiers for the output signals of the accelerometers. With developments to date, it is possible to eliminate the servoamplifier and accelerometer boxes and place the microelectronics aboard the platform.

Figure 2 shows one-half of the sliding contacts at a gimbal point. Servo signals from the platform pass

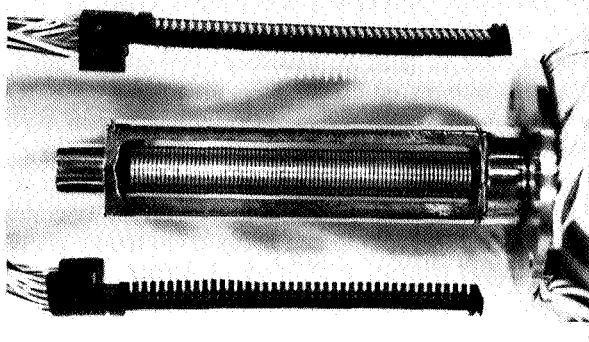


FIGURE 2. GIMBAL PIVOT SLIP RING

through the contacts to the amplifier box and back onto the platform to the torquers. Placing the electronics aboard the platform would greatly reduce the required number of sliding contacts and hence improve reliability. In addition, a tremendous amount of wiring, cabling, and interconnecting plugs would be eliminated.

MINIATURIZATION OF SPECIFIC CIRCUITS

The top row of modules in Figure 3 is the discrete component version of servoelectronics in use at present. The second row down is a hybrid version consisting of some integrated circuits complemented by discrete components. This was a step in developing the near totally integrated version as shown in the bottom row. A servoamplifier now occupies a volume of approximately 920 cubic centimeters (56 cubic inches). The integrated version can be packaged in approximately 16.4 cubic centimeters (one cubic inch). One package configuration being considered is a 6.03 centimeter (2 3/8 inch)-diameter disc 0.95 centimeter (3/8 inch) thick.

Figure 4 outlines the three major functional blocks of a servoamplifier.

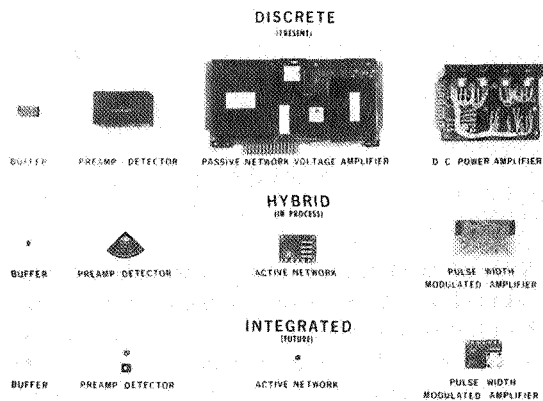


FIGURE 3. PLATFORM SERVO ELECTRONICS

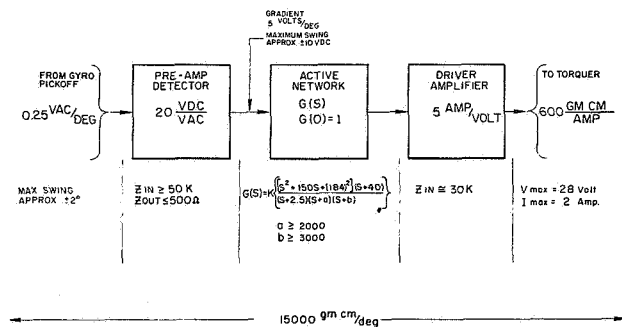


FIGURE 4. FUNCTIONAL BLOCK DIAGRAM

The preamplifier/demodulator, as shown in Figure 5, amplifies the gyro pickoff signal, demodulates with a full wave phase sensitive demodulator, and filters out the carrier ripple. This unit can easily be packaged in one-quarter of the 6.03 centimeter (2 3/8 inch)-disc configuration.

Figure 6 shows a phase and gain curve plot of a near complete integrated version of a network that will occupy even less than one-quarter of the 6.03 centimeter (2 3/8 inch) disc.

The power amplifier section can logically be divided into a modulator section and a power amplifier section as shown in Figure 7. This portion of the servoelectronics represents the greatest advancement. Both sections can be mounted in a quarter of the 6.03 centimeter (2 3/8 inch) disc. The power section is a complete bridge circuit made up of four

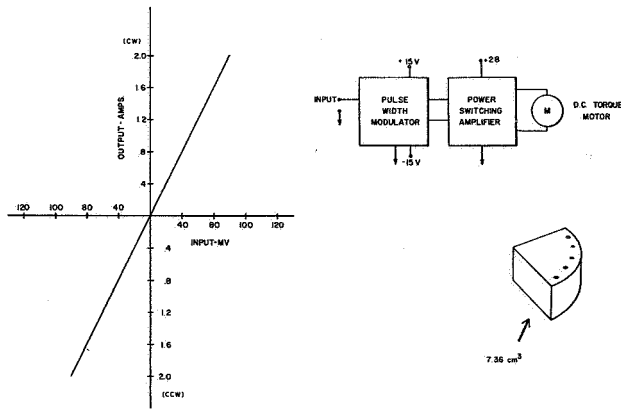


FIGURE 7. POWER AMPLIFIER SECTION

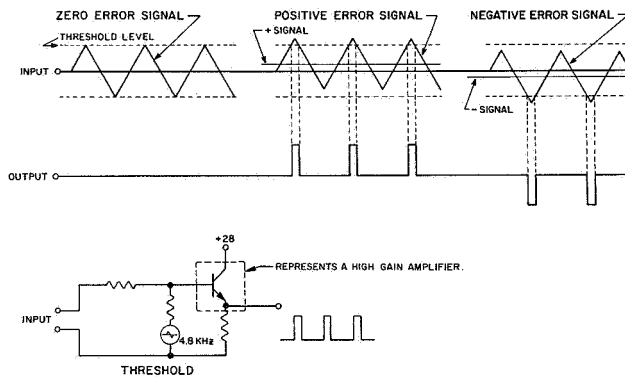


FIGURE 8. PULSE WIDTH MODULATION

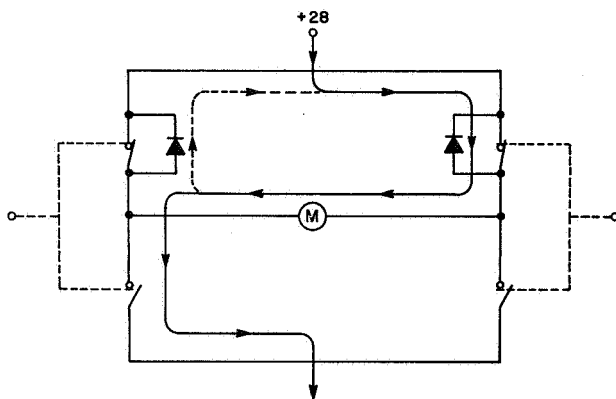


FIGURE 9. POWER BRIDGE

A number of applications, other than the servo-amplifier, can use this modulator and power switch. Some of these are the pulse width modulated power

control, the dc to dc converter, and the output stage of a static inverter.

Some electronics, other than that of the platform servos, have been miniaturized. Figure 10 shows

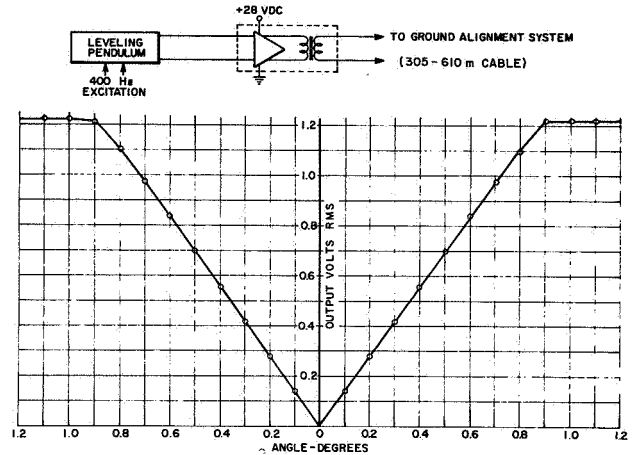


FIGURE 10. INTEGRATED PENDULUM PREAMPLIFIER

the block diagram and performance curve of a single chip monolithic integrated amplifier. In this case an isolation transformer is required to prevent ground loops between the vehicle and GSE batteries. Figure 11 shows the packaging with at least a 5 to 1 reduction in size.

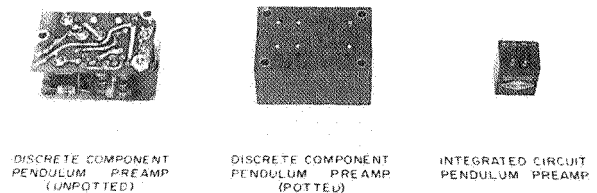


FIGURE 11. PLATFORM SERVO ELECTRONICS (POTTED & UNPOTTED)

Another area of achievement is the electronics for the PIGA encoder output. Figure 12 shows in block form one signal channel of which there are four on each accelerometer. As shown earlier, the wave shaping amplifiers were in the accelerometer-signal-conditioner box. As shown in Figure 13, all the electronics for the four encoder channels can be placed on the accelerometer.

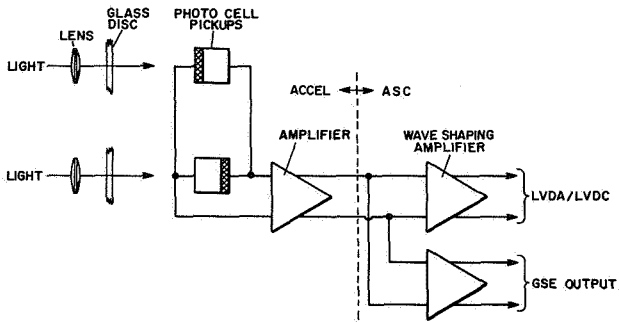


FIGURE 12. ACCELEROMETER OUTPUT CHANNEL

CONCLUSION

Microminiaturization of the platform electronics produces (1) increased reliability because of a 10/1 reduction in fixed interconnections (solder and weld), a 3/1 reduction in pressure interconnections (plugs and slip rings), and a 10/1 reduction in the number of elements; (2) electrically equal or better performance by better element matching and thermal tracking, and less noise and cross-talk on shorter leads and cables; (3) overall 100/1 size and weight reductions; (4) up to 10/1 cost reduction; (5) feasibility of redundancy; and (6) results of the program that are directly applicable to other inertial systems applicable to GSE as new designs are required, and innovations directly applicable in industry.



FIGURE 13. PLATFORM SERVO ELECTRONIC ACCELERATOR



INTEGRATED CIRCUITS IN TELEMETRY SYSTEMS

By

T. C. Lawson

SUMMARY

Operation of the Saturn V vehicle's instrumentation system requires a highly reliable and flexible telemetry system that can also be easily adaptable to future programs such as the Apollo Applications Program (AAP).

The development work now being conducted to achieve such a system is presented. New equipment for greater system flexibility, such as a telemetry data compressor, is discussed. Improvements in existing equipment by using integrated circuits for superior reliability are also presented to include modernization of multiplexers and pulse code modulation equipment.

INTRODUCTION

Today's critical and rapidly changing instrumentation requirements place severe demands upon the telemetry system. The Telemetry Branch at Marshall Space Flight Center is presently engaged in the design and development of a highly reliable, flexible telemetry system that will meet the instrumentation requirements of the Saturn V vehicle and be easily adaptable to future programs such as the Apollo Applications Program (AAP). Existing designs are being made more reliable by using integrated circuitry that will be phased into the Saturn V and other programs. Also, new equipment is being designed for greater telemetry system flexibility.

PRESENT SYSTEM

The present telemetry system consists of approximately twelve pieces of equipment that can be interconnected in various ways to provide the instrumentation for processing both analog and digital measuring signals. Figure 1 shows a typical system used on the S-IB stage for vehicles SA-201 through SA-204. None of this equipment contains integrated circuits.

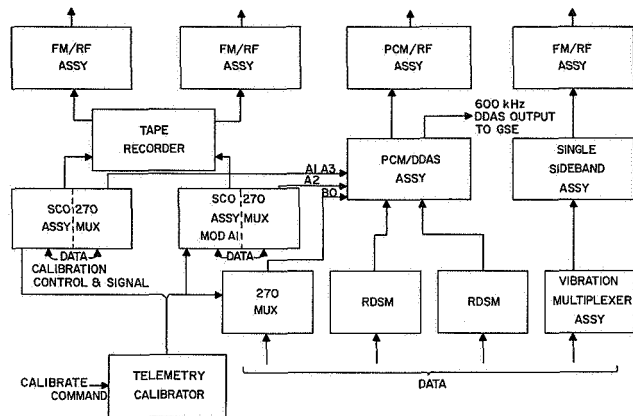


FIGURE 1. TYPICAL TELEMETRY SYSTEM

NEW DEVELOPMENTS

The pulse code modulation/digital data acquisition system (PCM/DDAS) (Fig. 1) must process many channels of information for transmission. Some of the information is rapidly changing and must be sampled often; while some remains fairly constant and only has to be monitored. To transmit the data that are not changing is an inefficient use of the RF spectrum.

A unit is being developed that will remove the redundant or repetitious data and thereby conserve bandwidth. This system will be inserted between the PCM/DDAS assembly and the output. Figure 2 is a flow diagram of this system.

When a new measurement is received by this system, the previous value for that particular measurement is recalled from memory along with a predetermined tolerance. The new and previous values are then compared. If the new value is equal to the previously transmitted value within the tolerance established for that particular measurement, the previously transmitted value is restored to memory and the system sequences to the next channel. No data are transmitted.

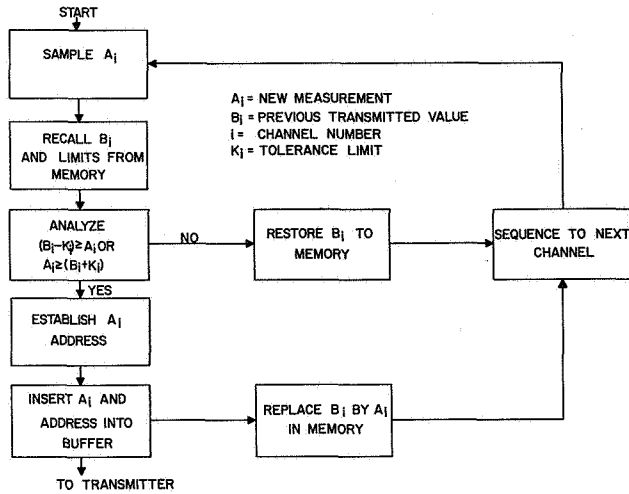


FIGURE 2. DATA COMPRESSOR

If the new value does not fall within the tolerance range of the previously transmitted value, an address is established for the new value. The address and value are inserted into a buffer and transmitted and stored in the memory in place of the previously transmitted value and its address. This design will result in either a reduction in bandwidth and the associated improved signal-to-noise ratio or will increase the amount of useful data that can be handled.

A prototype and two units capable of passing flight requirements have been constructed. Figure 3 shows the mechanical design and the complexity of the unit. Without integrated circuits, this equipment would not be feasible for flight use.

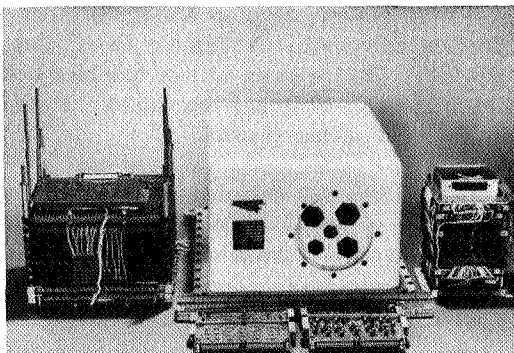


FIGURE 3. DATA COMPRESSOR

As shown in Figure 1, the 270 multiplexer requires many data input lines (up to 234). These inputs may be from remote parts of a stage on the vehicle. Integrated circuits result in improved reliability and reduction in weight of the electronic equipment, but some consideration must be given to the large amount of cabling mass with its many connections.

Figure 4 shows a new system under development that will group measurements in various locations of

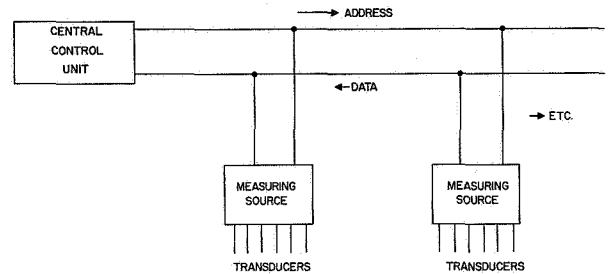


FIGURE 4. ADDRESSABLE TIME DIVISION DATA SYSTEM

the vehicle stage. A central control unit will transmit a channel address on a single address line to remotely placed measuring sources or multiplexers. The source containing the data of the transmitted address will then return the measurement to the central unit. The various measurements will time-share a single address line and a single data line.

Figure 5 shows the address system for the addressable time division data system. The central

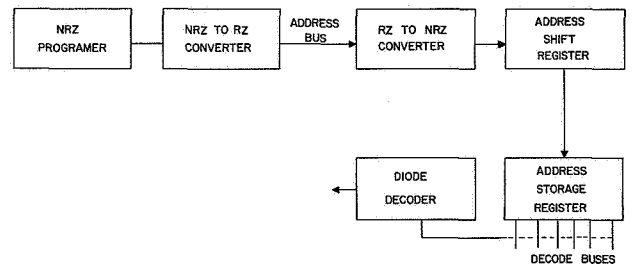


FIGURE 5. ADDRESS SYSTEM FOR THE ADDRESSABLE TIME DIVISION DATA SYSTEM

control unit generates the program in non return to zero (NRZ) form and converts it to a return to zero

(RZ) form for transmission. In the measuring source the RZ address is used to obtain a clock signal and is converted back to NRZ and transferred into an address shift register and then to a storage register. A diode network decodes the address information in the shift register and closes the addressed data gate. Transmission to the measuring source in the RZ form eliminates the need for a separate clock or oscillator in each multiplexer.

A feasibility breadboard using integrated circuits has been constructed and tested. Additional work is now being done on the address recognition circuit and the complete design is being assembled in flight configuration for final testing.

Use of this system will greatly reduce the number of cable connections and cable mass for sensors on remote parts of a stage.

In Figure 1 all the data processed in the PCM/DDAS system are shown being transmitted either on

the 600 kHz voltage controlled oscillator (VCO) line or by the PCM/RF transmitter. These data are sometimes required for use aboard the vehicle. A computer interface unit (CIU) is used to extract any desired data from the PCM/DDAS assembly, store it, condition it, and then present it to an onboard computer or other device when requested. This unit now exists in discrete form and is used in the Instrument Unit on the Saturn vehicle. Figure 6 is a block diagram of the system. Synchronization is provided by the PCM/DDAS assembly. An address is presented to the CIU by the computer, causing any previously stored information to clear. A data request signal is then applied. When the same address appears in the PCM/DDAS system as determined by the address comparators, the information for that address is transferred from the PCM/DDAS system into holding registers in the CIU and a data ready signal is transmitted to the computer. As long as the data request signal is present, the system will update itself every time the data are available. When the data request signal is removed, the last requested value will be stored and will be available to the computer until the address is changed.

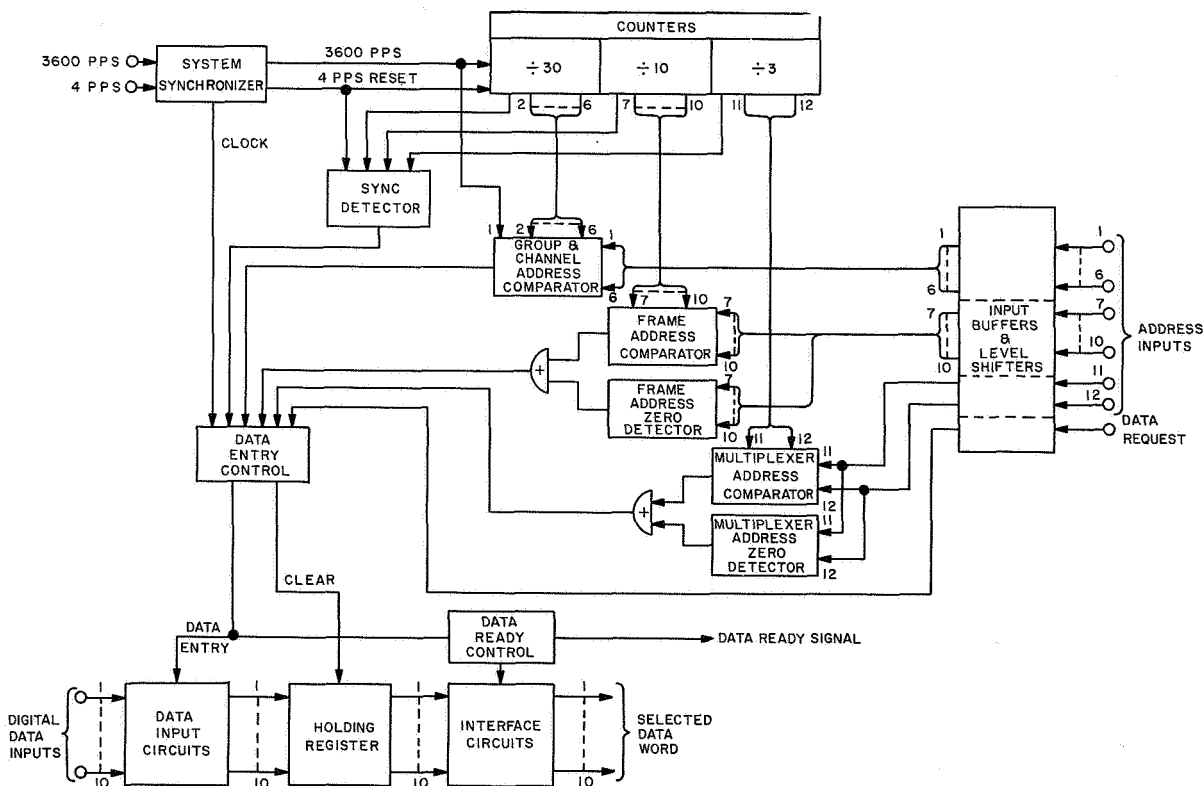


FIGURE 6. COMPUTER INTERFACE UNIT

An integrated circuit version is being developed that will improve the reliability and also permit more flexibility. The frequency of operation will be doubled to allow more data to be handled; pulse widths are being changed for use with equipment other than the onboard computer, such as an onboard data storage unit now being designed.

The new version will consist of monolithic integrated circuits except for the output stage and the power supply. The high voltage required at the output prohibits the use of present day integrated circuits.

Isolation between the PCM/DDAS system and the internal circuitry of the CIU will be accomplished by optics. This method will provide perfect isolation and yet will not involve transformers. The device to be used is an experimental Texas Instruments SNX1304 (Fig. 7) that consists of a gallium arsenide light emitter optically coupled to an integrated silicon photodetector feed-back-amplifier circuit. Common-mode rejection should also be very good.

One of the subsystems shown in Figure 1, the PCM/DDAS subsystem, processes data from a very

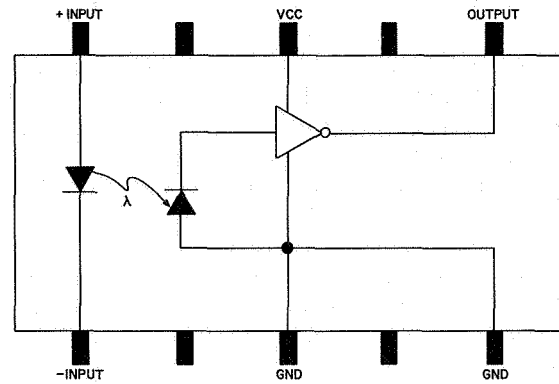


FIGURE 7. TEXAS INSTRUMENTS SNX1304 OPTOELECTRONIC PULSE AMPLIFIER

large number of sources. Its reliability is important in achieving overall reliability of the other subsystems that supply data to it. An integrated circuit version of this system has been designed that has essentially the same functional design as its discrete forerunner. Figure 8 is a block diagram of the system. The frequency of the clock will be doubled and the necessary

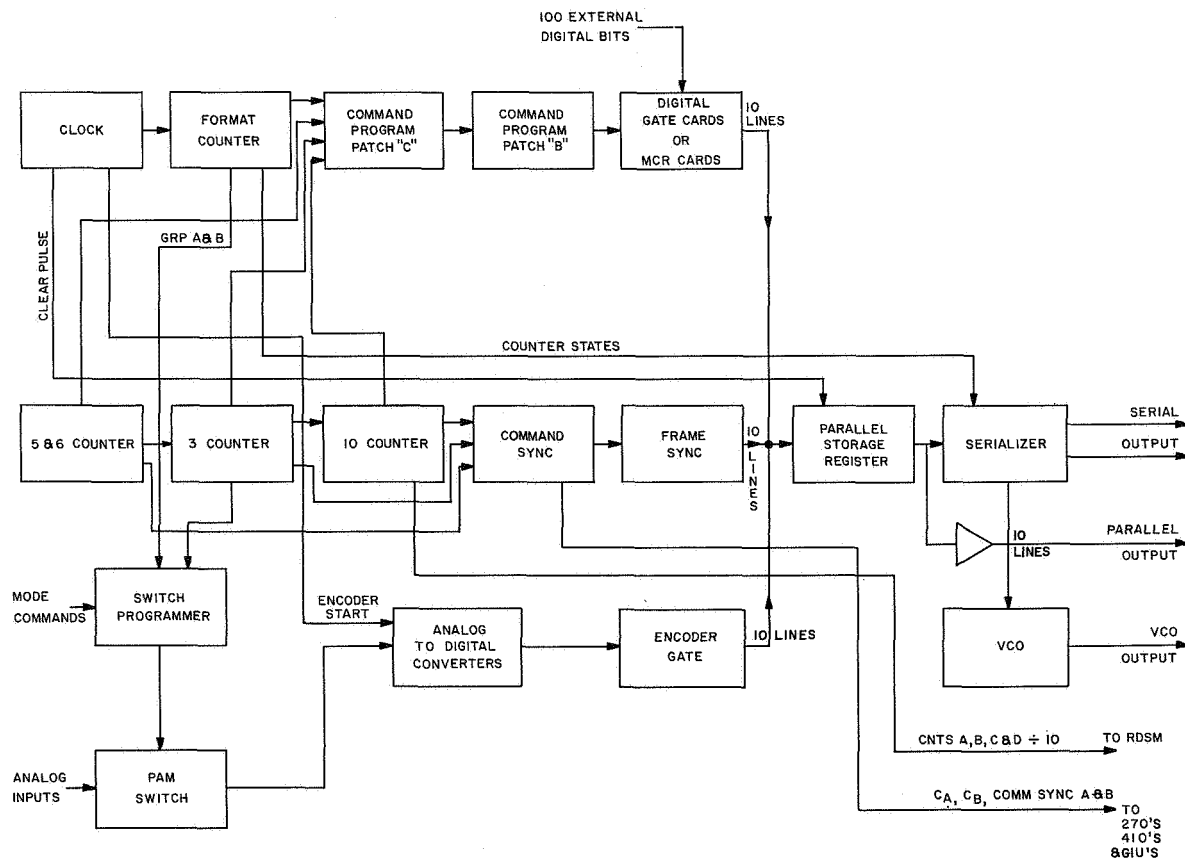


FIGURE 8. PCM/DDAS MODEL 302

circuitry will be added to permit doubling the amount of data that can be handled. The analog-to-digital (AD) converter will be left in its present discrete form because of the accuracy required; however, a program has been started to develop an integrated circuit AD converter.

Buffer amplifiers will be added to the parallel outputs in the integrated circuit version to provide better isolation between the serial and parallel outputs. In the present system, difficulty has been experienced when other equipment on the parallel outputs inserted spurious signals back into the serializer.

A new approach will be taken on some of the printed circuit boards in this development. The concentration of integrated circuits on a single layer or double-side printed circuit board is limited by the interconnecting lines rather than the components. Yet, many techniques used on multilayer boards are considered unreliable. Figure 9 is a cross section

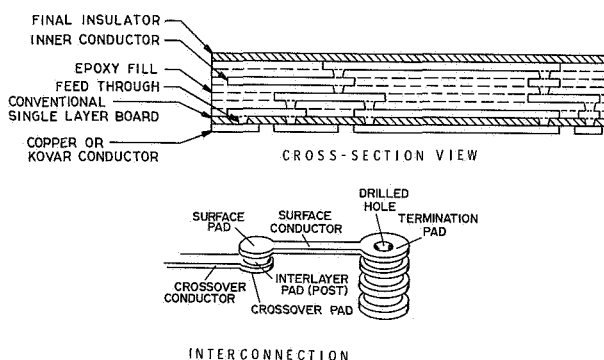


FIGURE 9. INTELLUX MULTILAYER BOARD

view of a board that should overcome most of the unreliable characteristics of multilayer boards. Manufacture of this board starts with a single layer board which is etched. The conductor is either copper or a weldable material, such as Kovar. Feed-through points are then etched through the epoxy insulator. The board is masked and the etched holes are filled by copper plating. The second layer circuit is next plated on, with masking, followed by an insulating layer. Feed-through points to the third layer are then etched, and so on for the remaining layers. The last insulating layer may be backed by a heat conducting material.

This type of fabrication yields a homogeneous mass for feed-through points that can be drilled for terminal posts. Interconnections of interlayers do

not use up valuable components mounting space on the top layer. This process will be used on the main interconnection board, or motherboard, and a few of the component boards.

This development is an interim approach since the AD converter requirements push integrated circuitry capabilities at this time. The existing unit is shown in Figure 10. The redesign will be packaged

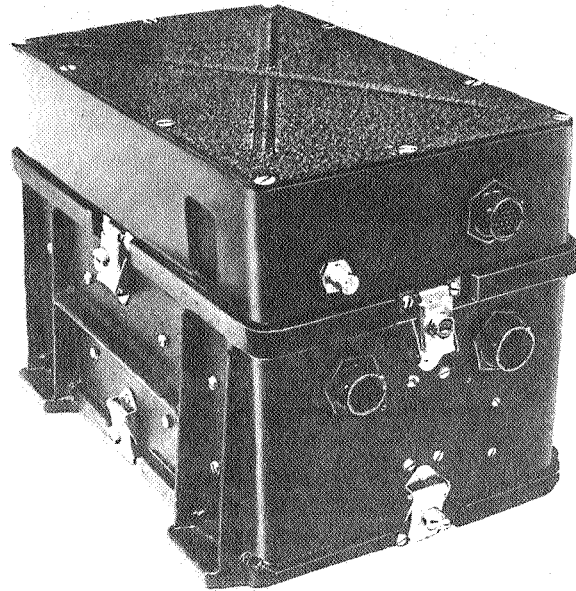


FIGURE 10. PCM/DDAS ASSEMBLY

entirely in the lower portion with the upper part removed. Even with this hybrid approach, the component count is reduced approximately 13:1, which should represent a considerable improvement in reliability.

The electrical design work is complete and a breadboard has been constructed and tested. Mechanical design is approximately 50 percent complete.

The 270 multiplexer requires a transformer to operate each data input channel. Transformers are considered one of the least reliable components of this system. In the present system, ten gates with their transformers are mounted on a printed circuit board. The buffer amplifier for the output of the gates and the transformer drivers are mounted on other boards. A new design using integrated circuits has been completed which will replace the transformers, the gates, the transformer drivers, and buffer amplifier. Figure 11 shows a comparison of the two versions. Gate drivers compatible with the

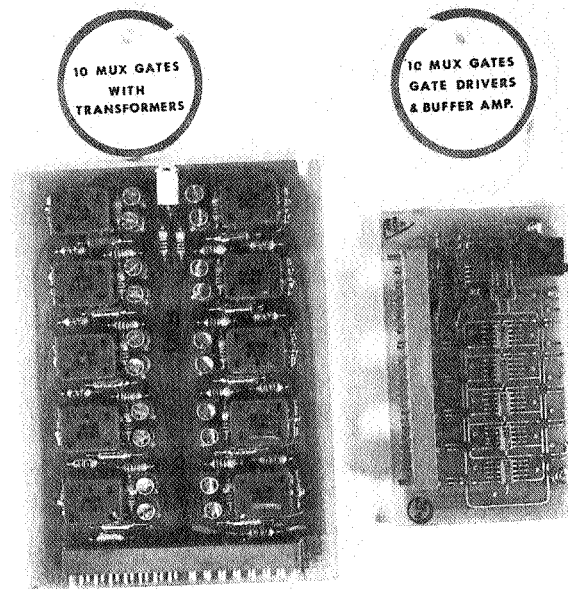


FIGURE 11. MULTIPLEXER GATES

Texas Instruments "51 series" were developed and are capable of driving either metallic oxide semi-conductors (MOS) or conventional field-effect gates. The present circuit employs conventional field-effect transistors (FET's). This new circuit has an error of approximately 0.06 percent of full scale over the temperature range of 253° K to 358° K, of which the major portion is in the buffer amplifier. This compares with the discrete version.

Now that a suitable gate is developed, the entire 270 multiplexer is being redesigned. Electrical design and breadboarding have been completed. Mechanical packaging has begun and will serve as a test for new packaging concepts.

Integrated circuit designs are resulting in up to a 20:1 reduction in the number of components, one of the main contributors to improved reliability. Fewer components require fewer connectors; therefore, a different mechanical approach must be taken in packaging integrated circuit telemetry systems. The next figures show the result of a packaging study which seems to offer an improvement in reliability from a mechanical viewpoint.

The integrated circuits will be mounted on small boards up to 5 centimeters (2 inches) square (Fig. 12). These boards will be grouped according to their function and interconnected by welding with flexible cable. The boards will have a damping

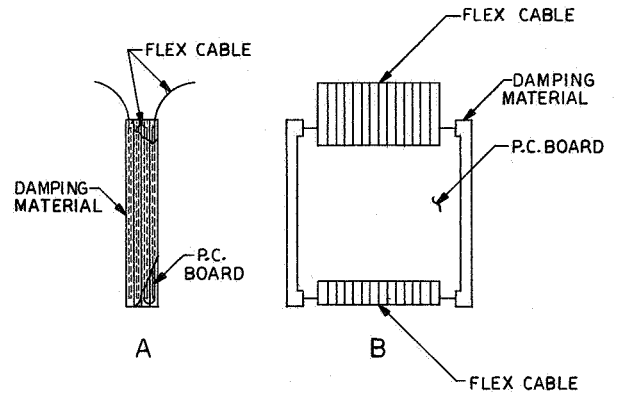


FIGURE 12. PRINTED CIRCUIT BOARD ASSEMBLY

material on each side edge and will be stacked together, with the damping material providing the separation. Figure 13 shows the accessibility of the boards after interconnection.

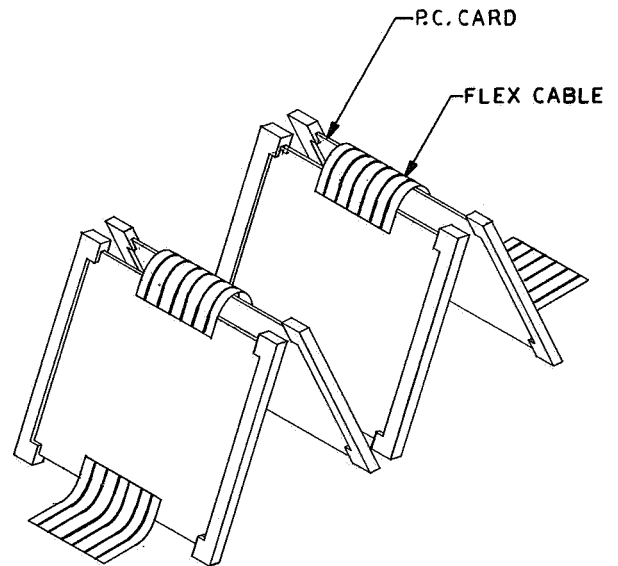


FIGURE 13. INTERCONNECTED PRINTED CIRCUIT BOARDS

Each group of boards will then fit tightly into a cavity as shown in Figure 14, and the groups will be interconnected by means of flex cable and a multilayer motherboard as shown in Figure 15. Holes in the motherboard over each cavity will allow a group to be extracted for troubleshooting. Full electrical check-out can also be accomplished before final assembly (Fig. 16) in the outer casting.

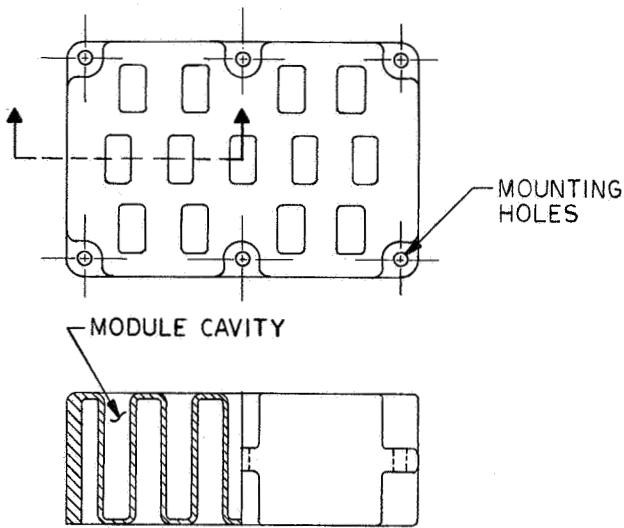


FIGURE 14. ELECTRONICS CHASSIS

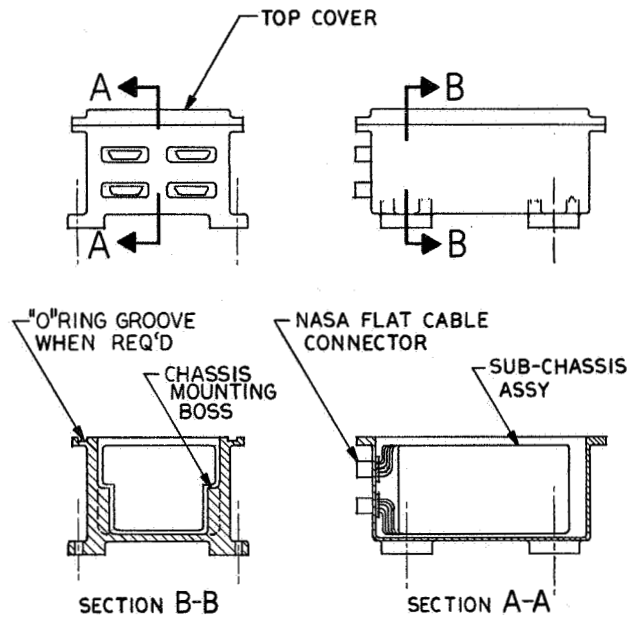


FIGURE 16. FINAL ASSEMBLY

Integrated circuits that will perform almost any logic function are being wired into a rack and the signal inputs and outputs are connected to patch sockets on a panel (Fig. 17). Figure 18 is a front view of the

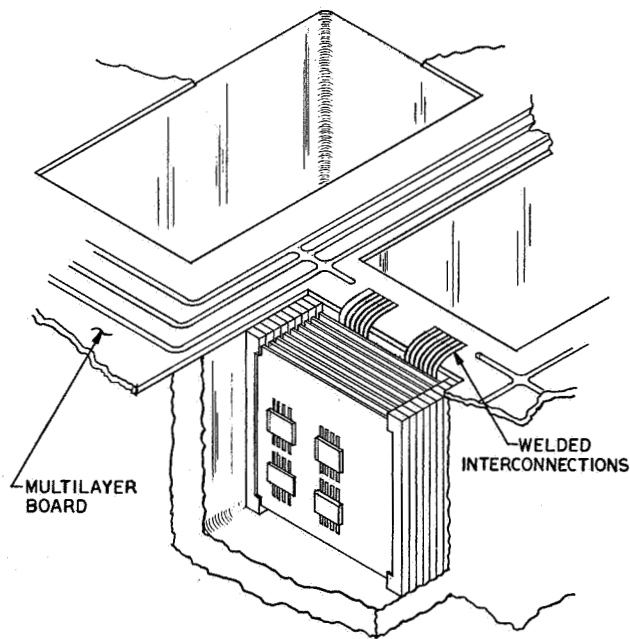


FIGURE 15. ELECTRONICS CHASSIS ASSEMBLY TECHNIQUE

This mechanical design should provide a reliable packaging technique and yet be easily accessible for electrical checkout.

Often it is desirable to prove out a logic design before incorporating it into a system. An integrated circuit patch board is being built for this purpose.

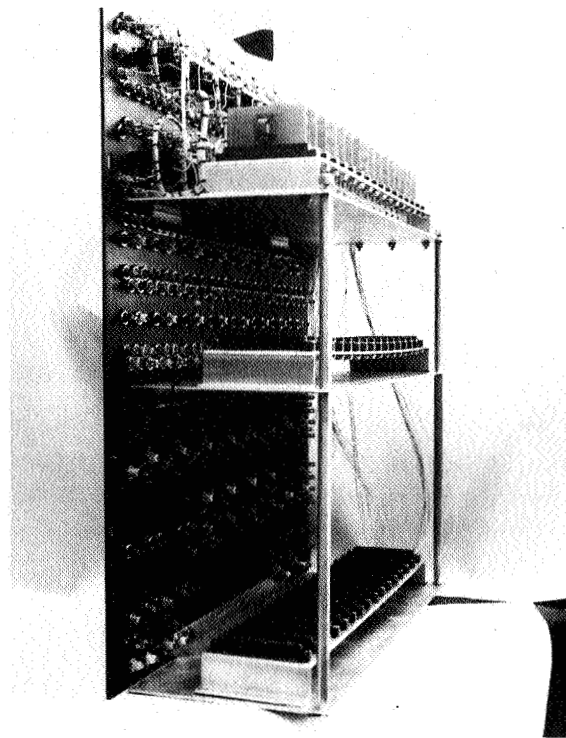


FIGURE 17. INTEGRATED CIRCUIT PATCH PANEL (REAR VIEW)

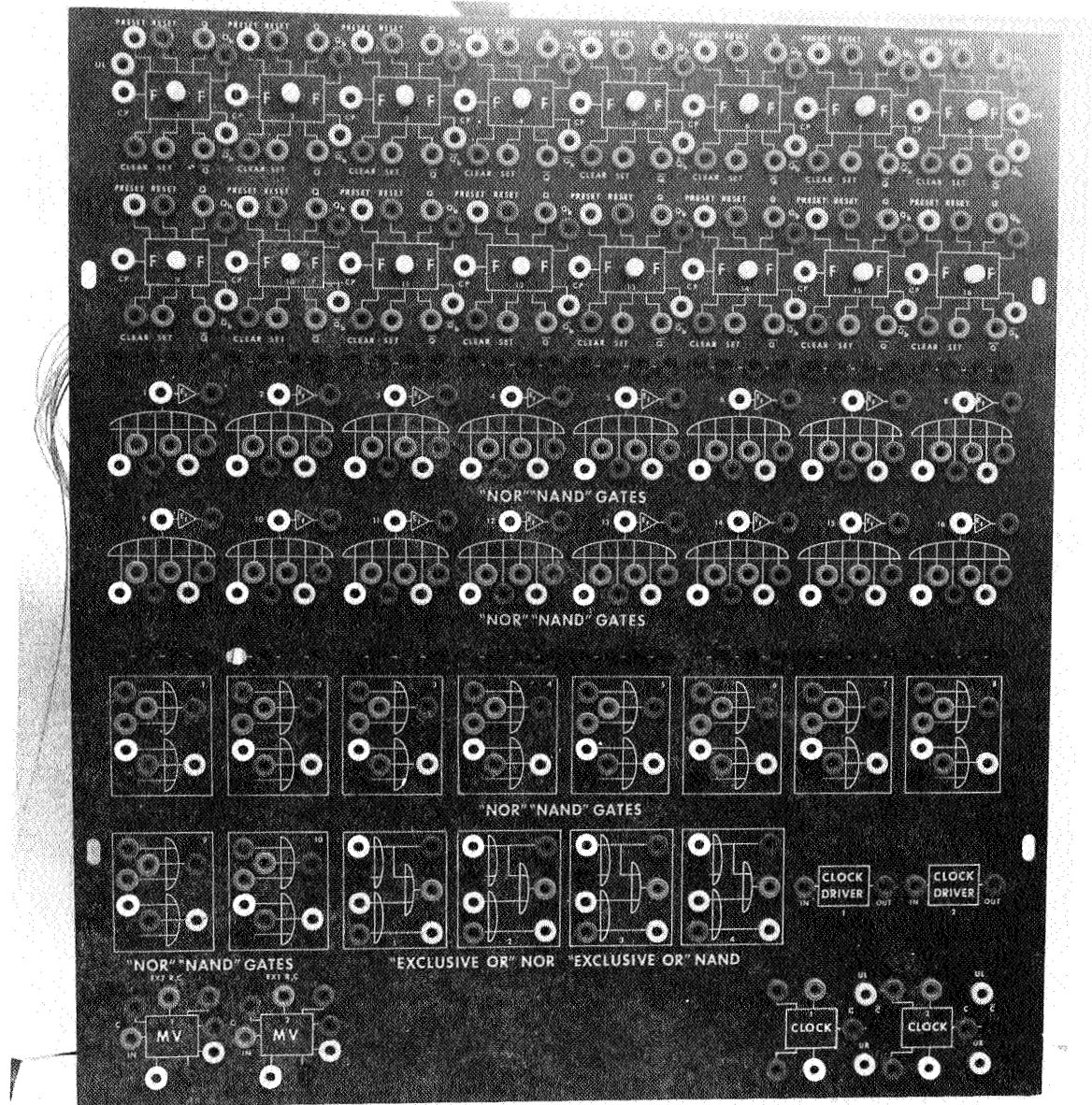


FIGURE 18. INTEGRATED CIRCUIT PATCH PANEL (FRONT VIEW)

panel. Transistorized indicator lights are connected to each flipflop to indicate its state. With the use of

patch cords, a simple logic circuit can be checked in a very short time.